MNRAS 000, 1–31 (2019) Preprint 14 March 2019 Compiled using MNRAS LATEX style file v3.0

The Dynamics and Distribution of Angular Momentum in HiZELS Star – Forming Galaxies at $z = 0.8 - 3.3$

S. Gillman,[1⋆] A. M. Swinbank,[1,2] A. L. Tiley,[1] C. M. Harrison,[9] Ian Smail,[1,2] U. Dudzevičiūtė,[1] R. M. Sharples,[1,3] P. N. Best,[7] R. G. Bower[1,2] R. Cochrane,[7,8] D. Fisher,[6] J. E. Geach,[12] K. Glazebrook,[6] Edo Ibar,[4] J. Molina,[14] D. Obreschkow,[10,11] M. Schaller,[2] D. Sobral,[5] S. Sweet,[6] J. W. Trayford[2,13] T. Theuns[2]

[1] *Centre for Extragalactic Astronomy, Durham University, South Road, Durham, DH1 3LE UK*
[2] *Institute for Computational Cosmology, Durham University, South Road, Durham DH1 3LE UK*
[3] *Centre for Advanced Instrumentation, Durham University, South Road, Durham DH1 3LE UK*
[4] *Instituto de Física y Astronomía, Universidad de Valparaíso, Avda. Gran Bretaña 1111, Valparaíso, Chile*
[5] *Department of Physics, Lancaster University, Lancaster, LA1 4BY, UK*
[6] *Centre for Astrophysics and Supercomputing, Swinburne University of Technology, PO Box 218, Hawthorn, VIC 3122, Australia*
[7] *SUPA, Institute for Astronomy, Royal Observatory Edinburgh, EH9 3HJ, UK*
[8] *Isaac Newton Group of Telescopes, E-38700 Santa Cruz de La Palma, Canary Islands, Spain*
[9] *European Southern Observatory, Karl-Schwarzschild-Str. 2, 85748 Garching b. Mnchen, Germany*
[10] *International Centre for Radio Astronomy Research (ICRAR), University of Western Australia, Crawley WA 6009, Australia*
[11] *ARC Centre of Excellence for All-Sky Astrophysics (CAASTRO), Australia*
[12] *School of Physics, Astronomy & Mathematics, University of Hertfordshire, College Lane, Hatfield, AL10 9AB, UK*
[13] *Leiden Observatory, Leiden University, P.O. Box 9513, 2300 RA Leiden, The Netherlands*
[14] *Departamento de Astronomia, Universidad de Chile, Casilla 36-D, Santiago, Chile*

Accepted 2019 March 12

ABSTRACT

We present adaptive optics assisted integral field spectroscopy of 34 star–forming galaxies at $z = 0.8$–3.3 selected from the HiZELS narrow-band survey. We measure the kinematics of the ionised interstellar medium on ∼1 kpc scales, and show that the galaxies are turbulent, with a median ratio of rotational to dispersion support of $V/\sigma = 0.82 \pm 0.13$. We combine the dynamics with high-resolution rest-frame optical imaging and extract emission line rotation curves. We show that high-redshift star forming galaxies follow a similar power-law trend in specific angular momentum with stellar mass as that of local late type galaxies. We exploit the high resolution of our data and examine the radial distribution of angular momentum within each galaxy by constructing total angular momentum profiles. Although the stellar mass of a typical star-forming galaxy is expected to grow by a factor ~ 8 in the ∼5 Gyrs between $z \sim 3.3$ and $z \sim 0.8$, we show that the internal distribution of angular momentum becomes less centrally concentrated in this period i.e the angular momentum grows outwards. To interpret our observations, we exploit the EAGLE simulation and trace the angular momentum evolution of star forming galaxies from $z \sim 3$ to $z \sim 0$, identifying a similar trend of decreasing angular momentum concentration. This change is attributed to a combination of gas accretion in the outer disk, and feedback that preferentially arises from the central regions of the galaxy. We discuss how the combination of the growing bulge and angular momentum stabilises the disk and gives rise to the Hubble sequence.

Key words: galaxies: evolution – galaxies: high redshift – galaxies: dynamics

1 INTRODUCTION

The galaxy population in the local Universe is dominated by two distinct populations, with ∼70% spirals, and ∼25%

⋆ E-mail: steven.r.gillman@durham.ac.uk

spheroidal and elliptical galaxies (Abraham & van den Bergh 2001). These two populations make up the long-defined classes of the Hubble sequence defined as late and early type galaxies (Hubble 1926; Sandage 1986). The differences are also reflected in many properties, including the galaxy integrated colours, star–formation rates, rotation velocity and velocity dispersion (e.g. Tinsley 1980; Kauffmann et al. 2003; Delgado-Serrano et al. 2010; Zhong et al. 2010; Whitaker et al. 2012; Aquino-Ortíz et al. 2018; Eales et al. 2018)

The two populations can be separated fundamentally by differences in the baryonic angular momentum. In a Λ cold dark matter (ΛCDM) Universe angular momentum originates from tidal torques between dark matter halos in the early Universe (Hoyle 1956). The amount of halo angular momentum acquired has a strong dependence on halo mass ($J \propto M_{halo}^{5/3}$) as predicted from tidal torque theory, as well as the epoch of formation ($J \propto t$) (e.g. Catelan & Theuns 1996). As the baryonic material within the halo cools and collapses, it should weakly (within a factor of two) conserve angular momentum, due to tensor invariance, and form a star forming disk. Subsequent gas accretion, star formation and feedback will redistribute the angular momentum within the disk, whilst mergers will preferentially remove angular momentum from the system (Mo et al. 1998).

Fall & Efstathiou (1980) demonstrated that the baryons in today's spiral galaxies must have lost $\sim 30\%$ of their initial angular momentum, most likely through secular processes and viscous angular momentum redistribution (Bertola & Capaccioli 1975; Burkert 2009; Romanowsky & Fall 2012). In contrast, in early types (spheroids) the initial angular momentum of the baryons must have been redistributed (or lost) to the halo, most efficiently through major mergers. As first suggested by Fall (1983), stellar angular momentum in galaxies is predicted to follow power-law-scaling between specific stellar angular momentum ($j_\star = J_*/M_*$) and stellar mass ($M_\star$) where local spiral galaxies follow a scaling with $j_\star \propto M_\star^{2/3}$ (e.g. Romanowsky & Fall 2012; Cortese et al. 2016).

Recent studies of low-redshift galaxies have expanded upon these works showing that the specific angular momentum and mass also correlate with total bulge to disc ratio (B/T) of the galaxy (e.g. Obreschkow & Glazebrook 2014; Fall & Romanowsky 2018; Sweet et al. 2018). Indeed, galactic disks and spheroidal galaxies occupy independent regions of the $j_\star$–$M_\star$–B/T plane, suggesting they were formed via distinct physical processes. Major mergers play a minimal role in disk galaxies' evolution, whilst elliptical galaxies' histories are often dominated by major mergers, stripping the galaxy of gas required for star formation and disk creation, as shown in observational studies (Cortese et al. 2016; Posti et al. 2018; Rizzo et al. 2018) and hydro-dynamical simulations (Lagos et al. 2017; Trayford et al. 2018).

Two of the key measurements required to follow the formation of today's disk galaxies are: how is the angular momentum within a baryonic galaxy (re)distributed; and which physical processes drive the evolution such that the galaxies evolve from turbulent systems at high redshift into rotation-dominated, higher angular momentum, low redshift galaxies.

At high redshift star–forming galaxies are clumpy and turbulent, and whilst showing distinct velocity gradients (e.g. Förster Schreiber et al. 2009a, 2011b; Wisnioski et al. 2015), they are typically dominated by 'thick' discs and irregular morphologies. Morphological surveys (e.g. Conselice et al. 2011; Elmegreen et al. 2014), as well as hydrodynamical simulations (e.g. Trayford et al. 2018) highlight that a critical epoch in galaxy evolution is $z \sim 1.5$. This is when the spiral galaxies (that would lie on a traditional Hubble classification) become as common as peculiar galaxies. If one of the key elements that dictates the morphology of a galaxy is angular momentum, as suggested by the studies of local galaxies (e.g. Shibuya et al. 2015; Cortese et al. 2016; Elson 2017) then this would imply that this is the epoch when the internal angular momentum of star-forming galaxies is becoming sufficiently high to stabilise the disk (Mortlock et al. 2013).

Observationally we can test whether the emergence of galaxy morphology at this epoch is driven by the increase in the specific angular momentum of the young stars and star forming gas. A star–forming galaxy with a given rotation velocity but lower angular momentum will have a smaller stellar disk, high surface density and assuming the gas is Toomre unstable the gaseous disk will have a higher Jeans mass (Toomre & Toomre 1972). This results in more massive star–forming clumps which can be observed in the ionised-gas (e.g. Hα) morphology (e.g. Genzel et al. 2011; Livermore et al. 2012; Förster Schreiber et al. 2014).

Integral field spectroscopy studies of $z = 1-2$ star forming galaxies also show that galaxies with increasing Sérsic index have lower specific angular momentum, where sources with the highest specific angular momentum, for a given mass, have the most disc-dominated morphologies (e.g. Burkert et al. 2016; Swinbank et al. 2017; Harrison et al. 2017). Measuring the resolved dynamics of galaxies at high redshift on ~ 1 kpc scales allows us to go beyond a measurement of size and asymptotic rotation speed, examining the radial distribution of the angular momentum, comparing it to the distribution of the stellar mass.

Numerical studies (e.g. Van den Bosch et al. 2002; Lagos et al. 2017) further motivate the need to study the internal (re)distribution of angular momentum of gas disks with redshift, and suggest that the majority of the evolution occurs within the half stellar mass radius of the galaxy. Resolving galactic disks on kpc-scales in the distant Universe presents an observational challenge. At $z \sim 1.5$ galaxies have smaller half light radii ($\sim 2-5$ kpc; Ferguson et al. 2004; Stott et al. 2013) which equate to $\sim 0\farcs2-0.5''$. The typical resolution of seeing-limited observations is $\sim 0.7''$. To measure the internal dynamics on kilo-parsec scales (which are required to derive the shape and normalisation of the rotation curve within the disk, with minimal beam smearing effects) requires very high resolution, which, prior to the James Webb Space Telescope (JWST; García Marín et al. 2018), can only be achieved with adaptive optics. The advent of adaptive optics (AO) integral field observations at high redshift allows us to map the dynamics and distribution of star formation on kpc-scale in distant galaxies (e.g. Genzel et al. 2006; Cresci et al. 2007; Wright & Larkin 2007; Genzel et al. 2011; Swinbank et al. 2012b; Livermore et al. 2015; Molina et al. 2017; Schreiber et al. 2018; Circosta et al. 2018; Perna et al. 2018).

In this paper we investigate the dynamics and both total and radial distribution of angular momentum in high redshift galaxies, and explore how this evolves with cosmic time. The data comprises of adaptive optics observations of

34 star–forming galaxies from $0.8 \leq z \leq 3.3$ observed with the OH-Suppressing Infrared Integral Field Spectrograph (OSIRIS; Larkin et al. 2006), the Spectrograph for INtegral Field Observations in the Near Infrared (SINFONI; Bonnet et al. 2004a) and the Gemini Northern Integral Field Spectrograph (Gemini-NIFS; McGregor et al. 2003). Our targets lie in the SA22 (Steidel et al. 1998), UKIDSS Ultra-Deep Survey (UDS; Lawrence et al. 2007) and Cosmological Evolution Survey (COSMOS; Scoville et al. 2007) extra-galactic fields (Appendix B Table B1). The sample brackets the peak in cosmic star formation and the high resolution $\lesssim$0.″1 observations allow the inner regions of the galaxies to be spatially resolved. Just over two thirds of the sample have Hα detections whilst the remaining third were detected at $z\sim$3.3 via [OIII] emission. All of the galaxies lie in deep extragalactic fields with excellent multi-wavelength data, and the majority were selected from the HiZELS narrow–band survey (Sobral et al. 2013a), and have a nearby natural guide or tip–tilt star to allow adaptive optics capabilities.

In Section 2 we describe the observations and the data reduction. In Section 3 we present the analysis used to derive stellar masses, galaxy sizes, inclinations and dynamical properties. In Section 4 we combine stellar masses, sizes and dynamical measurements to infer the redshift evolution of the angular momentum in the sample. We derive the radial distributions of angular momentum within each galaxy and compare our findings directly to a stellar mass and star-formation rate selected sample of EAGLE galaxies. We discuss our findings and give our conclusions in Section 5.

Throughout the paper, we use a cosmology with Ω_Λ=0.73, Ω_m=0.30 and H_0=70 km s^{-1} Mpc^{-1} (Planck Collaboration et al. 2018). In this cosmology a spatial resolution of 1 arcsecond corresponds to a physical scale of 8.25 kpc at a redshift of $z = 2.2$ (the median redshift of the sample.) All quoted magnitudes are on the AB system and stellar masses are calculated assuming a Chabrier IMF (Chabrier 2003).

2 OBSERVATIONS & DATA REDUCTION

The majority of the observations, (31 targets; 90% of the sample)[1], were obtained from follow up spectroscopic observations of the High Redshift Emission Line Survey (HiZELS; Geach et al. 2008; Best et al. 2013) which targets Hα emitting galaxies in five narrow ($\Delta z = 0.03$) redshift slices: $z = 0.40$, 0.84, 1.47, 2.23 & 3.33 (Sobral et al. 2013a). This panoramic survey provides a luminosity-limited sample of Hα and [OIII] emitters spanning $z = 0.4$–3.3 Exploiting the wide survey area, the targets from the HiZELS survey were selected to lie within 25.″0 of a natural guide star to allow for adaptive optics capabilities. The sample span the full range of the rest-frame $(U - V)$ and rest-frame $(V - J)$ colour space as well as the stellar mass and star formation rate plane of the HiZELS parent sample (Appendix A Table A1 and Figure 1). The data were collected from August 2012 to December 2017 from a series of observing runs on SINFONI (VLT), NIFS (Gemini North Observatory) & OSIRIS (Keck) integral field spectrographs (see Appendix B Table B1 for details).

Our sample includes the galaxies first studied by Swinbank et al. (2012a) and Molina et al. (2017), who analysed the dynamics and metallicity gradients in twenty galaxies from our sample. In this paper we build upon this work and including 14 new sources, of which 9 galaxies are at $z > 3$. We also combine observations of the same galaxies from different spectrographs in order to maximise the signal to noise of the data.

2.1 VLT / SINFONI

To map the Hα and [OIII] emission in the galaxies in our sample, we undertook a series of observations using the Spectrograph for INtegral Field Observations in the Near Infrared (SINFONI; Bonnet et al. 2004a). SINFONI is an integral field spectrograph mounted at the Cassegrain focus of UT4 on the VLT and can be used in conjunction with a curvature sensing adaptive optics module (MACAO; Bonnet et al. 2004b). SINFONI's wavelength coverage is from 1.1–2.45μm, which is ideally suited for mapping high redshift Hα and [OIII] emission.

SINFONI employs an image slicer and mirrors to reformat a field of 3.″0 × 3.″0 with a pixel scale of 0.″05. At $z = 0.84$, 1.47 and 2.23 the Hα emission line is redshifted to $\sim$1.21μm, 1.61μm and 2.12μm, into the J, H and K-bands respectively. The [OIII] emission line at $z \sim 3.33$ is in the K–band at 2.16μm. The spectral resolution in each band is $\lambda/\Delta\lambda$ ~4500. Each observing block (OB) was taken in an ABBA observing pattern (A=Object frame, B=Sky frame) with 1.″5 chops to sky, keeping the target in the field of view. We undertook observations between 2009 September 10 and 2016 August 01 with total exposure times ranging from 3.6ks to 13.4ks (Appendix B Table B1) where each individual exposure was 600s. All observations were carried out in dark time with good sky transparency and with a closed–loop adaptive optics correction using natural guide stars.

In order to reduce the SINFONI data the ESOREX pipeline was used to extract, wavelength calibrate and flat field each spectra and form a data cube from each observation. The final data cube was generated by aligning the individual observing blocks, using the continuum peak, and then median combining them and sigma clipping the average at the 3-σ level to reject pixels with cosmic ray contamination. For flux calibration, standard stars were observed each night either immediately before or after the science exposures. These were reduced in an identical manner to the science observations.

2.2 Gemini / NIFS

The Gemini Northern Integral Field Spectrograph (Gemini-NIFS; McGregor et al. 2003) is a single object integral field spectrograph mounted on the 8 m Gemini North telescope which we used in conjunction with the adaptive optics system ALTAIR. NIFS has a 3.″0 × 3.″0 field of view and an image slicer which divides the field into 29 slices with angular sampling of 0.″1 × 0.″04. The dispersed spectra from

[1] Three galaxies are taken from the KMOS Galaxy Evolution Survey (KGES; Tiley et al, in prep), a sample of ~300 star forming galaxies at $z \sim 1.5$. Their selection was based on Hα detections in the KMOS observations and the presence of a tip–tilt star of $M_H < 14.5$ within 40.″0 of the galaxy to make laser guide star adaptive optics corrections possible.

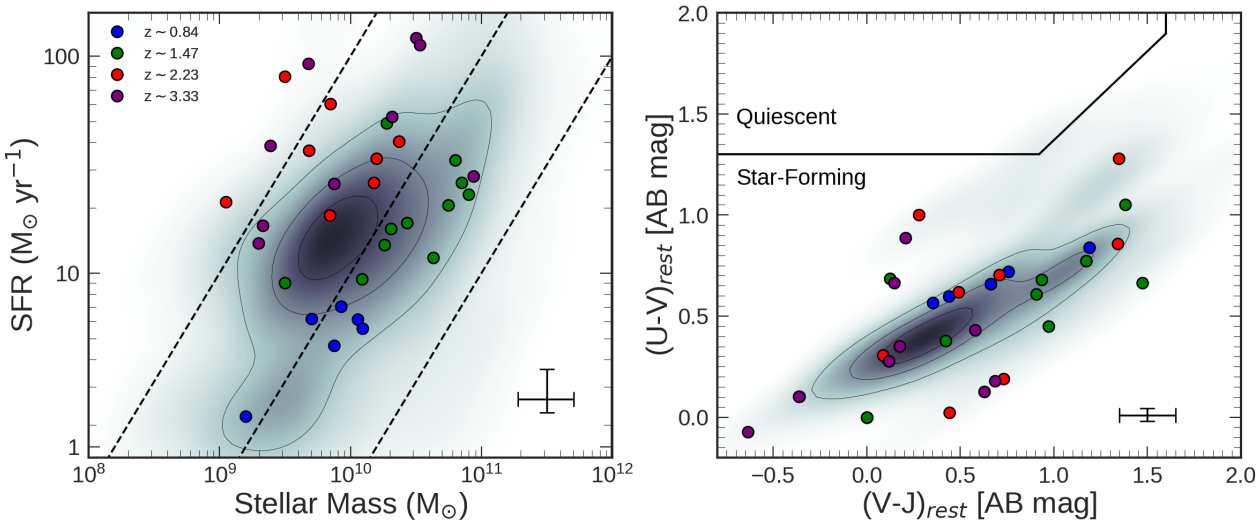

Figure 1. *Left:* The Hα and [OIII] dust-corrected star formation rate of each galaxy as function of stellar mass derived deriving from MAGPHYS. The HiZELS sample is shown as the grey shaded region whilst our sample is coloured by redshift. Adopted 0.2 dex stellar mass uncertainty and median fractional star formation rate uncertainties are indicated by black lines. We show tracks of constant specific star formation rate (sSFR) with sSFR = 0.1, 1 and 10 Gyr^{-1}. This shows that our sample cover a broad range of stellar mass and star formation rates, *Right:* The rest-frame $(U-V)$ colour as a function of rest-frame $(V-J)$ colour for our sample and galaxies in the HiZELS survey, demonstrating that the galaxies in our sample cover the full range of HiZELS galaxies colour-colour parameter space. Median uncertainties in $(V-J)$ and $(U-V)$ colour indicated by black lines. The Williams et al. (2009) boundary (black wedge) separates quiescent galaxies (top left) from star-forming galaxies (bottom right).

the slices are reformatted on the detector to provide two-dimensional spectra imaging using the K–band grism covering a wavelength range of $2.00-2.43\mu$m. All of our observations were undertaken using an ABBA sequence in which the 'A' frame is an object frame and the 'B' frame is a 6 arcsecond chop to blank sky to enable sky subtraction. Individual exposures were 600s and each observing block 3.6ks, which was repeated four times resulting in a total integration time of 14.4ks per target.

The NIFS observations were reduced with the standard Gemini IRAF NIFS pipeline which includes extraction, sky-subtraction, wavelength calibration and flat-fielding. Residual OH sky emission lines were removed using sky subtraction techniques described in Davies (2007). The spectra were then flux calibrated by interpolating a black body function to the spectrum of the telluric standard star. Finally data cubes for each individual exposure were created with an angular sampling of $0\farcs05 \times 0\farcs05$. These cubes were then mosaicked using the continuum peak as reference and median combined to produce a single final data cube for each galaxy. The average FWHM of the point spread function (PSF) measured from the telluric standard star in the NIFS data cubes is $0\farcs13$ with spectral resolution of $\lambda/\Delta\lambda \sim 5290$.

The three galaxies in our sample observed with NIFS also have SINFONI AO observations. We stacked the observations from different spectrographs, matching the spectral resolution of each, in order to maximise the signal to noise. In the stacking procedure, each observation was weighted by its signal to noise. The galaxy SHIZELS–21 is made up of two NIFS (14.6ks, 15.6ks) and one SINFONI (9.6ks) observation whilst SHIZELS–23 and SHIZELS–24 are the median combination of one NIFS (15.6ks) and one SINFONI (12.0ks) observation. On average the median signal-to-noise per pixel increased by a factor of ~ 2 as a result of stacking the frames and the redshift of the Hα emission lines in the individual and stack data cubes agreed to within $\leq 0.01\%$.

2.3 Keck / OSIRIS

We also include in our sample three galaxies observed with the OH-Suppressing Infrared Integral Field Spectrograph (OSIRIS; Larkin et al. 2006) which are stellar mass, star formation rate and kinematically selected based on the KMOS observations, from the KGES survey (Tiley et al. 2019, Gillman et al. in prep.). The OSIRIS spectropgraph is a lenslet integral field unit that uses the Keck Adaptive Optics System to observe from $1.0-2.5\mu$m on the 10 m Keck I Telescope. The AO correction is achieved using a combination of a Laser Guide Star (LGS) and Tip–Tilt Star (TTS) to correct for atmospheric turbulence down to $0\farcs1$ resolution in a rectangular field of view of order $4\farcs0 \times 6\farcs0$ (Wizinowich et al. 2006).

Observations were carried out on 2017 December 06 and 07. Each exposure was 900s, dithering by $3\farcs2$ in the Hn4, Hn3 and Hn1 filters to achieve good sky subtraction while keeping the galaxy within the OSIRIS field of view. Each OB consists of two AB pairs and for each target a total of four AB pairs were observed equating to 7.2ks in total. Each AB was also jittered by predefined offsets to reduce the effects of bad pixels and cosmic rays.

We used the OSIRIS data reduction pipeline version 4.0.0 using rectification matrices taken on 2017 December 14 and 15, to reduce the OSIRIS observations. The pipeline removes crosstalk, detector glitches and cosmic rays per frame, to later combine the data into a cube. Further sky subtrac-

tion and masking of sky lines was also undertaken in targets close to prominent sky lines, following procedures outlined in Davies (2007). Each reduced OB was then centred, trimmed, aligned and stacked with other OBs to form a co–added fully reduced data cube of an object. On average each final reduced data cube was a combination of four OBs.

In total 25 Hα and 9 [OIII] detections were made using the SINFONI, NIFS and OSIRIS spectrographs from $z\sim0.8-3.33$, full details of which are given in Appendix A Table A1. A summary of the observations are given in Appendix B Table B1 .

2.4 Point Spread Function Properties

It is well known that the adaptive optics corrected point spread function diverges from a pure Gaussian profile (e.g. Baena Gallé & Gladysz 2011; Exposito et al. 2012; Schreiber et al. 2018), with a non-zero fraction of power in the outer wings of the profile. In order to measure the intrinsic nebula emission sizes of the galaxies in our sample we must first construct the point spread function for the integral field data using the standard star observations taken in conjunction with the science frames. We centre and median combine the standard star calibration images, deriving a median point spread function for the J, H and K wavelength bands.

We quantify the the half-light radii of the these median point spread functions using a three-component Sérsic model, with Sérsic indices fixed to be a Gaussian profile ($n=0.5$). The half-light radii, R_h, of the PSF is derived using a curve of growth analysis on the three component Sérsic model's two-dimensional light profile. We derive the median PSF R_h for the J, H and K bands where $R_h=0\farcs18\pm0\farcs05$, $0\farcs14\pm0\farcs03$ and $0\farcs09\pm0\farcs01$ respectively. The integral field PSF half-light radii in kilo-parsecs is shown in Appendix B Table B1. We convolve half-light radii of the median PSF in each wavelength band with the intrinsic size of galaxies in our sample when extracting kinematic properties from the integral field data (e.g Section 3.8 & 3.5). The median Strehl ratio achieved for our observations is 33% and the median encircled energy within $0\farcs1$ is 25% (the approximate spatial resolution is $0\farcs1$ FWHM, 825 pc at $z\sim2.22$, the median redshift of our sample).

3 ANALYSIS

With the sample of 34 emission-line galaxies with adaptive optics assisted observations assembled, we first characterise the integrated properties of the galaxies. In the following section we investigate the stellar masses and star formation rates, sizes, dynamics, and their connection with the galaxy morphology, placing our findings in the context of the general galaxy population at these redshifts. We first discuss the stellar masses and star formation rates which we will also use in Section 3.4 when investigating how the dynamics evolve with redshift, stellar mass and star formation rate.

3.1 Star–Formation Rates and Stellar Masses

Our targets are taken from some of the best studied extragalactic fields with a wealth of ancillary photometric data available. This allows us to construct spectral energy distributions (SEDs) for each galaxy spanning from the rest-frame UV to mid-infrared with photometry from Ultra-Deep Survey Almaini et al. (2007), COSMOS Muzzin et al. (2013) and SA22 Simpson et al. (2017).

To measure the galaxy integrated properties we use the MAGPHYS code to fit the $UV-8\,\mu$m photometry (e.g. da Cunha et al. 2008, 2015), from which we derive stellar masses and extinction factors (A_v) for each galaxy. The full stellar mass range of our sample is $\log(M_*[M_\odot])=9.0-10.9$ with a median of $\log(M_*[M_\odot])=10.1\pm0.2$. We compare the stellar masses of our objects to those previously derived in Sobral et al. (2013a) finding a median ratio of $M_*^{\rm MAGPHYS}$ / $M_*^{\rm SOBRAL}=1.07\pm0.23$, indicating the MAGPHYS stellar masses are slightly higher than those derived from simple interpretation of galaxy colours alone. However we employ a homogeneous stellar mass uncertainty of ±0.2 dex throughout this work that should conservatively account for the uncertainties in stellar mass values derived from SED fitting of high-redshift star-forming galaxies (Mobasher et al. 2015).

The star formation rates of $z<3$ galaxies in our sample were derived from the Hα emission line fluxes presented in Sobral et al. (2013a). We correct the Hα flux assuming a stellar extinction of $A_{H\alpha}=0.37$, 0.33 & 0.07 for $z=0.84$, 1.47 & 2.23, the median derived from MAGPHYS SED fitting. Correcting to a Chabrier initial mass function and following Wuyts et al. (2013) to convert between stellar and gas extinction and the methods outlined Calzetti et al. (2000), we derive extinction corrected star formation rates for each galaxy. The uncertainties on the star formation rates are derived from bootstrapping the 1σ uncertainties on the Hα emission line flux outlined in Sobral et al. (2013a). For the 9 [OIII] sources in our sample, we adopt the star formation rates and uncertainties derived in Khostovan et al. (2015).

The median star formation rate of our sample is $<$SFR$>=22\pm4$ $M_\odot yr^{-1}$ with a range from SFR$=2-120$ $M_\odot yr^{-1}$. However, our observational flux limits mean that the median star formation evolves with redshift with $<$SFR$>=6\pm1$, 13 ± 5, 38 ± 8 & 25 ± 10 $M_\odot yr^{-1}$ for $z=0.84$, 1.47, 2.23 & 3.33. The median star formation rate of our Hα detected galaxies is comparable, within uncertainties, to the knee of the HiZELS star formation rate function at each redshift (SFR*) with SFR$^*=$ 6, 10 & 25 $M_\odot yr^{-1}$ at $z=0.84$, 1.47 & 2.23, as presented in Sobral et al. (2014).

The stellar masses and star formation rates for the sample are shown in Figure 1. As a comparison we also show the HiZELS population star-formation and stellar masses, derived in the same way, and tracks of constant specific star formation rate (sSFR) with sSFR = 0.1, 1 and 10 Gyr^{-1}. A clear trend of increasing star formation rate at fixed stellar mass with redshift is visible. We note that the galaxies in our sample at $z=1.47$ typically have the highest stellar masses, and as shown by Cochrane et al. (2018), the HiZELS population at $z=1.47$ is at higher L/L^* than the $z=0.84$ or $z=2.23$ samples. The star formation rate and stellar mass for each galaxy are shown in Appendix A Table A1. We also show the distribution of rest-frame $(U-V)$ colour as a function of rest-frame $(V-J)$ colour for our sample in Figure 1. The HiZELS population is shown for comparison, indicating that our galaxies cover the full range of the HiZELS population colour distribution. Based on the above, we conclude that the galaxies in our sample at $z=0.84$, 2.23 and

& 3.33 are representative of the star formation rate - stellar mass relation at each redshift, whilst galaxies at $z = 1.47$ lie slightly above this relation.

3.2 Galaxy Sizes

Next we turn our attention to the sizes of the galaxies in our sample. All of the galaxies in the sample were selected from the extra-galactic deep fields, either UDS, COSMOS or SA22. Consequently there is a wealth of ancillary broadband data from which the morphological properties of the galaxy can be derived (Stott et al. 2013; Paulino-Afonso et al. 2017). The observed near−infrared emission of a galaxy is dominated by the stellar continuum. At our redshifts, the observed near−infrared samples the rest frame 0.4 − 0.8 μm emission and is always above the 4000$\AA$ break so is less likely to be affected by sites of on-going intense star formation. Therefore parametric fits to the near−infrared photometry are more robust than Hα measurements for measuring the 'size' of a galaxy. For just over half the sample (21 galaxies) we exploit *HST* imaging, the majority of which is in the near-infrared (F140W, F160W) or optical (F606W) bands at 0.″12 resolution. The remainder is in the F814W band at 0.″09 resolution. All other galaxies, in SA22 and UDS, have ground based K−band imaging with sampling of 0.″13 per pixel and PSF of 0.″7 FWHM from the UKIRT Infrared Deep Sky Survey (UKIDDS; Lawrence et al. 2007).

To measure the observed stellar continuum size and galaxy morphology, we first perform parametric single Sérsic fits to the broadband photometric imaging of each galaxy. To account for the point spread function (PSF) of the image, we generate a PSF for each image from a stack of normalised unsaturated stars in the frame. We build two-dimensional Sérsic models of the form:

$$\mathrm{I(R)} = \mathrm{I_e exp}\left(-\mathrm{b_n}\left[\left(\frac{\mathrm{R}}{\mathrm{R_h}}\right)^{(1/\mathrm{n})} - 1\right]\right), \quad (1)$$

and use the MPFIT function (Markwardt 2009) to convolve the PSF and model in order to optimise the Sérsic parameters including the axis ratio (Sérsic 1963).

Since the galaxies can be morphologically complex and to provide a non-parametric comparison to the Sérsic half-light radii, we also derive half light radii numerically within an aperture two times the Petrosian radius ($2\mathrm{R_p}$) of the galaxy. The Petrosian radius is derived by integrating the broadband image light directly and is defined by $\mathrm{R_p}$=1.5×$\mathrm{R}_{\eta=0.2}$ where $\mathrm{R}_{\eta=0.2}$ is the radius (R) at which the surface brightness at R is one fifth of the surface brightness within R (e.g. Conselice et al. 2002). This provides a non parametric measure of the size which is independent of the mean surface brightness. The half light radius, $\mathrm{R_h}$, is then defined as the radius at which the flux is one half of that within $2\mathrm{R_p}$ deconvolved with the PSF.

For the 21 galaxies with *HST* imaging we measure $\mathrm{R_h}$ in both ground and *HST* based photometry, both parametrically (Figure 2) and non-parametrically. To test how well we recover the sizes in ground-based measurements alone we compare the ground based continuum half light radii to the *HST* continuum half light radii, deriving a median ratio of $<\mathrm{R_h^G/R_h^{HST}}> = 0.97 \pm 0.05$. Applying the same parametric fitting procedure to the remaining galaxies we derive

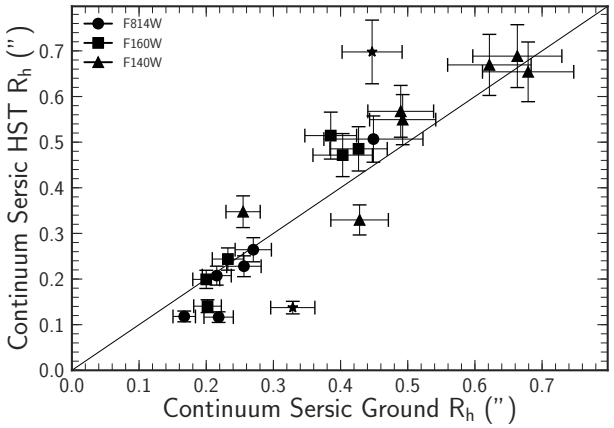

Figure 2. The half-light radius derived from Sérsic function fits to both ground based and *HST* data in Near-IR bands, for 21 galaxies in our sample. Marker shape represents the *HST* filter, star points indicate galaxies where ground and *HST* photometry show different morphological features or defects. The majority of sizes show good agreement with $<\mathrm{R_h^G/R_h^{HST}}>$=0.97 ± 0.05, independent of the band of the observation.

half-light radii for all 34 galaxies with $< R_\mathrm{h} > = 0.''43 \pm 0.''06$, which equates to 3.55 ± 0.50 kpc at $z = 2.22$ (the median redshift of the sample). Numerically we derive a median of $< R_\mathrm{h} > = 0.''55 \pm 0.''04$ (4.78 ± 0.41 kpc at the z=2 .22), with $<\mathrm{R_h^{Sérsic}}>/\mathrm{R_h^{Numerical}} > = 0.82 \pm 0.04$, indicating that the non-parametric fitting procedure broadly reproduces the parametric half-light radii. The median continuum half light size derived for our sample from Sérsic fitting is comparable to that obtained by Stott et al. (2013) for HiZELS galaxies out to $z = 2.23$, with $< R_\mathrm{h} > = 3.6 \pm 0.3$ kpc.

We further test the reliability of the recovered sizes (and their uncertainties), by randomly generating 1000 Sérsic models with $0.5 < n < 2$ and $0.''1 < \mathrm{R_h} < 1.''0$. These models are convolved with the UDS image point spread function and Gaussian random noise is added appropriate for the range in total signal-to-noise for our observations. Each model is then fitted to derive 'observed' model parameters. We recover a median size of $<\mathrm{R_h^{True}}>/\mathrm{R_h^{Obs}} > = 0.99 \pm 0.05$ and Sérsic index $<\mathrm{n_{True}/n_{Obs}} > = 1.05 \pm 0.07$. This demonstrates our fitting procedures accurately derives the intrinsic sizes of the galaxies in our sample. From this point forward we take the parametric Sérsic half-light radii as the intrinsic $\mathrm{R_h}$ of each galaxy.

As a test of the expected correlation between continuum size and the extent of nebular emission (e.g. Bournaud et al. 2008; Förster Schreiber et al. 2011a), we calculate the Hα (O[III] for galaxies at $z > 3$) half light radii of the galaxies in the sample. We follow the same procedures as the continuum stellar emission, but using narrow band images generated from the integral field data. We model the PSFs, using a stack of unsaturated stars that were observed with the spectrographs at the time of the observations using a multi-component Sérsic ($n = 0.5$) model.

We derive both parametric and non-parametric half-light radii from Sérsic fitting and numerical analysis within $2\mathrm{R_p}$. For the full sample of 34 galaxies the median parametric nebula half-light radii is $<\mathrm{R_h^{Nebula}} > = 0.''31 \pm 0.''06$ with

$<R_h^{Sérsic}>/R_h^{Numerical} >= 0.93 \pm 0.04$. The nebula emission sizes on average are consistent with the continuum stellar size, with $<R_h^{Continuum}>/R_h^{Nebula} >= 1.15 \pm 0.19$. We note that the low-surface brightness of the outer regions of the high-redshift galaxies may account for the apparent ∼10% smaller nebula sizes in our sample.

3.3 Galaxy Inclination and Position angles

To derive the inclination of the galaxies in our sample we first measure the ratio of semi–minor (b) and major (a) axis from the parametric Sérsic model. We derive an uncertainty on the axis ratio of each galaxy by bootstrapping the fitting procedure over an array of initial conditions. For galaxies that are disk-like, the axis ratio is related to the inclination by:

$$\cos^2(\theta_{inc}) = \frac{\left(\frac{b}{a}\right)^2 - q_0^2}{1 - q_0^2}, \quad (2)$$

where $\theta_{inc} = 0$ represents a face-on galaxy. The value of q_0, which accounts for the fact that galaxy disks are not infinitely thin, depends on galaxy type, but is typically in the range of $q_0 = 0.13 - 0.20$ for rotationally supported galaxies at $z \sim 0$ (e.g. Weijmans et al. 2014). We adopt $q_0 = 0.2$ to be consistent with other high redshift integral field surveys (KROSS; Harrison et al. 2017, KMOS3D; Wisnioski et al. 2015). The full range of axis ratio in the sample is $b/a = 0.2 - 0.9$ with $<b/a> = 0.69 \pm 0.04$ corresponding to a median inclination for the sample of $< \theta_{inc} > = 48^\circ \pm 3^\circ$.

3.4 Emission Line Fitting

Next we derive the kinematics, rotational velocity and dispersion profiles of the galaxies by performing emission line fits to the spectrum in each data cube.

For the Hα and [NII] doublet (25) sources we fit a triple Gaussian profile to all three emission lines simultaneously, whilst for [OIII] emitters a single Gaussian profile is used when we model the [OIII] λ5007 emission line. We do not have significant detections of the λ4959 [OIII] or λ4862 Hβ emission line. The fitting procedure uses a five or six parameter model with redshift, velocity dispersion, continuum and emission line amplitude as free parameters. For the Hα emitting galaxies we also fit the [NII]/Hα ratio, constrained between 0 and 1.5. The FWHM of the emission lines are coupled, the wavelength offsets fixed and the flux ratio of the [NII] doublet ($\frac{[NII]\lambda6583}{[NII]\lambda6548}$) fixed at 2.8 (Osterbrock & Ferland 2006). We define the instrumental broadening of the emission lines from the intrinsic width of the OH sky lines in each galaxy's spectrum, by fitting a single Gaussian profile to the sky line. The instrumental broadening of the OH sky lines in the J, H and K bands are $\sigma_{int} = 71\,km\,s^{-1} \pm 2\,km\,s^{-1}$, $50\,km\,s^{-1} \pm 5\,km\,s^{-1}$ and $39\,km\,s^{-1} \pm 1\,km\,s^{-1}$ respectively. The initial parameters for spectral fitting are estimated from spectral fits to the galaxy integrated spectrum summed from a 1.″0 aperture centred on the continuum centre of the galaxy.

We fit to the spectrum in 0.″15 × 0.″15 (3 × 3 spaxels) spatial bins, due to the low signal-to-noise in individual spaxels, and impose a signal-to-noise threshold of S/N ≥ 5 to the fitting procedure. If this S/N is not achieved we bin the spectrum over a larger area until either the S/N threshold is achieved or the binning limit of 0.″35 × 0.″35 is reached (∼1.5 × the typical AO-corrected psf width). In Figure 3 we show example Hα and [OIII] intensity, velocity and velocity dispersion for five galaxies in the sample.

3.5 Rotational Velocities

We use the Hα and [OIII] velocity maps to identify the kinematic major axis for each galaxy in our sample. We rotated the velocity maps around the continuum centre in 1° steps, extracting the velocity profile in 0.15 arcsecond wide slits and calculating the maximum velocity gradient along the slit. We bootstrap this process, adding Gaussian noise to each spaxel's velocities of order the velocity error derived from emission line fitting. The position angle with the greatest bootstrap median velocity gradient was identified as being the major kinematic axis (PA_{vel}), as shown by the blue line in Figure 3.

By extracting the velocity profile of the galaxies in our sample about the kinematic major axis, we are assuming the galaxy is an infinitely thin disk with minimal non-circular motions and is kinematically 'well-behaved'. We note however that this may not be true for all galaxies in sample, with some galaxies having significant non-circular motions leading to an underestimate of the rotation velocity and an overestimate of the velocity dispersion in these galaxies.

The accuracy of the velocity profile extracted for each galaxy depends on the accuracy to which the kinematic major axis is identified. To quantify the impact on the rotation velocity profile of deriving an incorrect kinematic position angle, we extract the rotation profiles of our galaxies about there broadband semi-major axis as well as there kinematic axis. On average we find minimal variation between $Vrot_{BB}(r)$ and $Vrot_{KE}(r)$ with $< Vrot_{BB}(r)/Vrot_{KE}(r) > = 0.94 \pm 0.15$.

In order to minimise the impact of noise on our measurements, we also fit each emission line rotation velocity curve (v) with a combination of an exponential disk (v_D) and dark matter halo (v_H). We use these models to extrapolate the data in the outer regions of the galaxies' velocity field, as opposed to interpreting the implications of the individual model parameters. For the disk dynamics we assume that the baryonic surface mass density follows an exponential profile (Freeman 1970) and the halo term can be modelled as a modified Navarro, Frenk & White (NFW) profile (Navarro et al. 1997). The halo velocity model converges to the NFW profile at large distances and, for suitable values of r_0, it can mimic the NFW or an isothermal profile over the limited region of the galaxy which is mapped by the rotation curve. The dynamics of the galaxy are described by the following disk and halo velocity components:

$$v^2 = v_D^2 + v_H^2,$$

$$v_D^2(x) = \frac{1}{2}\frac{GM_d}{R_d}(3.2x)^2(I_0K_0I_1K_1),$$

$$v_H^2(r) = \frac{6.4G\rho_0 r_0^3}{r}\left(\ln(1+\frac{r}{r_0}) - \tan^{-1}(\frac{r}{r_0}) + \frac{1}{2}\ln[1+(\frac{r}{r_0})^2]\right),$$

where $x = R/R_d$ and I_n and K_n are the modified Bessel functions computed at $1.6x$ with M_d and R_d as the disk

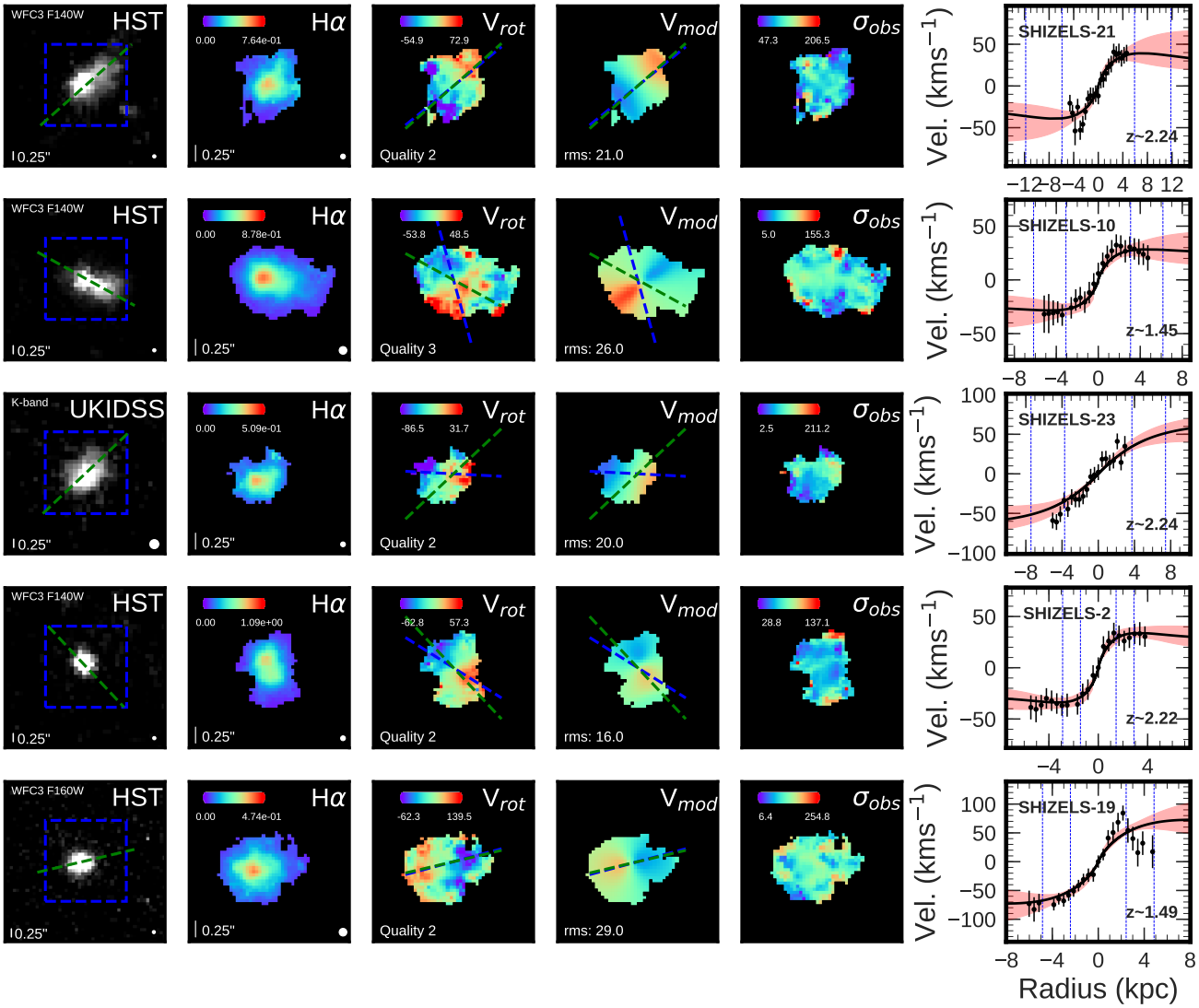

Figure 3. Example of spatially resolved galaxies in our sample. From left to right; Broadband photometry of the galaxy (left), with PA_{im} (green dashed line) and data cube field of view (blue dashed square). Hα or [OIII] flux map, velocity map, velocity model and velocity dispersion map, derived from the emission line fitting. PA_{vel} (blue dashed line) and PA_{im} (green dashed line) axes plotted on the velocity map and model. Rotation curve extracted about kinematic position axis (right). Rotation curve shows lines of R_h and $2R_h$ derived from Sérsic fitting, as well 1σ error region (red) of rotation curve fit (black line).

mass and disk scale length respectively. In fitting this model to the rotation profiles, there are strong degeneracies between R_d, ρ_0 and r_0. To derive a physically motivated fit, we modified the dynamical model to be a function of the dark matter fraction, disk scale radius and disk mass. Using the stellar mass, derived in Section 3, as a starting parameter for the disk mass, enables the fitting routine to converge. The dynamical centre of the galaxy was allowed to vary in the fitting procedure by having velocity and radial offsets as free parameters constrained to $\pm 20\,\mathrm{km\,s^{-1}}$ and ± 0.1 arcseconds. The dark matter fraction in galaxy with a given disk and dark matter mass is given by:

$$f_{DM} = \frac{M_{\rm DM}}{M_{\rm d} + M_{\rm DM}},$$

where the dark matter mass and disk mass are derived from;

$$M_{DM}(<R) = \int_0^R \rho(r) 4\pi r^2 dr = \int_0^R \frac{4\pi\rho_0 r_0^3 r^2}{(R+r_0)(R^2+r_0^2)} dr,$$

$$M_d(<R) = \int_0^R e^{-\frac{r}{R_d}} 2\pi r dr,$$

The dynamical model therefore contains five free parameters, M_d, R_d, f_{DM}, V_{off} and r_{off} where V_{off} and r_{off} are velocity and radial offsets for the rotation curve to allow for continuum centre uncertainties. We use the MCMC package designed for PYTHON (EMCEE; Foreman-Mackey et al. 2013), to perform Markov Chain Monte Carlo sampling with 500 walkers, initial burn-in of 250 and final steps to convergence of 500. We then use a χ^2 minimisation method to quantify the uncertainty on the rotational velocity extracted from the

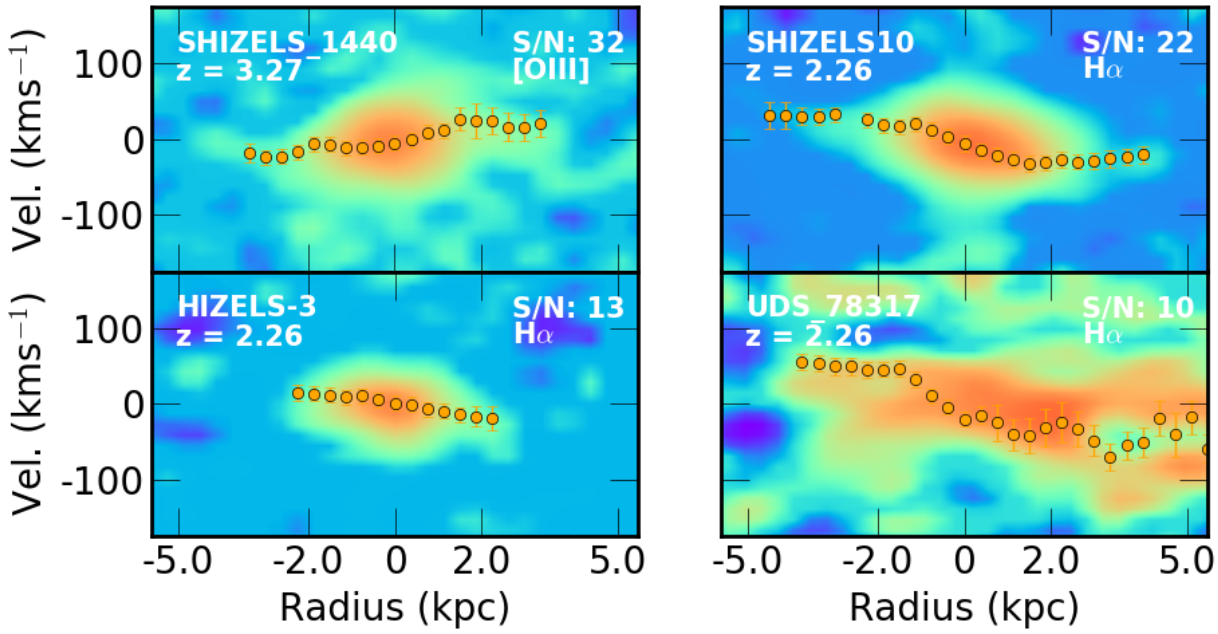

Figure 4. The position-velocity diagrams of four galaxies in the sample extracted from a slit about the kinematic major axis of each galaxy. The galaxies shown are selected from bins of emission line S/N derived from the galaxies integrated spectrum. We overlay each galaxies ionised gas rotation curve as derived in Section 3.4 for comparison. Redshift, emission line and S/N of each position-velocity map is shown, with upper left to bottom right as high to low galaxy integrated S/N.

model. The 1σ error is defined as the region in parameter space where the $\delta\chi^2 = |\chi^2_{\rm best}$ - $\chi^2_{\rm params}| \leq$ number of parameters. Prior to the MCMC procedure we apply the radial and velocity offsets to the rotation to reduce the number of free parameters and centre the profiles. The parameter space for 1σ uncertainty is thus $\delta\chi^2 \leq 3$. Taking the extremal velocities derived within the $\delta\chi^2 \leq 3$ parameter space provides the uncertainty on $V_{\rm rot}$. The rotation velocities and best fit dynamical models are shown in Figure 3. The full samples kinematics are shown in Appendix D. To show the full extent of the quality of data in our sample, we derive position-velocity diagrams for each galaxy. In Figure 4 we show one position-velocity diagram from each quartile of galaxy integrated signal to noise with the galaxies ionised gas rotation curve overlaid.

Next we measure the rotation velocities of our sample at $2R_{\rm h}$ ($=3.4$ $R_{\rm d}$ for an exponential disk) (e.g. Miller et al. 2011). For each galaxy we convolve $R_{\rm h}$ with the PSF of the IFU observation and extract velocities from the rotation curve. At a given radii our measurement is a median of the absolute values from the low and high components of the rotation curve. Finally we correct for the inclination of the galaxy, as measured in Section 3.2. On average the extraction of $Vrot_{2R_{\rm h}}$ from each galaxy's rotation curve requires extrapolation from the last data point ($R_{\rm last}$) to $2R_{\rm h}$ in our sample, where the median ratio is $< R_{\rm last}/2R_{\rm h} > = 0.42 \pm 0.04$. However for the sample, the average $Vrot_{2R_{\rm h}}$ is $\sim$14% smaller than the velocity of the last data point ($V_{\rm last}$) with $< V_{\rm last}/Vrot_{2R_{\rm h}} > = 1.14 \pm 0.11$ which is within 1σ. Figure 5 shows the distribution of radial and velocity ratios.

To quantify the impact of beam smearing on the rotational velocity measurements, we follow the methods of Johnson et al. (2018), and derive a median ratio of $< R_{\rm d} \,/\, R_{\rm h}^{\rm PSF} > = 2.17 \pm 0.18$ which equates to an average rotational velocity correction of 1 %. We derive the correction for each galaxy in the sample and correct for beam smearing effects. Appendix C Table C1 displays the inclination, beam smearing corrected rotation velocity ($Vrot_{2R_{\rm h}}$) for each galaxy. The full distribution of $R_{\rm d} \,/\, R_{\rm h}^{\rm PSF}$is shown in Appendix E.

The median inclination beam smearing corrected rotation velocity in our is sample is $< Vrot_{2R_{\rm h}} > = 64 \pm 14\,{\rm km\,s^{-1}}$, with the sample covering a range of velocities from $Vrot_{2R_{\rm h}} = 17 - 380\,{\rm km\,s^{-1}}$. The SINS/ZC-SINF AO survey (Schreiber et al. 2018) of 35 star forming galaxies at $z \sim 2$ identify a median rotation velocity of $< V_{\rm rot} > = 181\,{\rm km\,s^{-1}}$, with a range of $V_{\rm rot} = 38 - 264\,{\rm km\,s^{-1}}$. This approximately a factor of three larger than our sample, although we note their sample selects galaxies of higher stellar mass with $\log(M_*[M_\odot]) = 9.3 - 11.5$ whereas our selection selects lower mass galaxies.

3.6 Kinematic Alignment

The angle of the galaxy on the sky can be defined as the morphological position angle ($PA_{\rm im}$) or the kinematic position angle ($PA_{\rm vel}$). High-redshift IFU studies (e.g. Wisnioski et al. 2015; Harrison et al. 2017) use the misalignment between the two position angles to provide a measure of the kinematic state of the galaxy. The (mis)alignment is defined such that:

$$\sin\Psi = |\sin(PA_{\rm im} - PA_{\rm vel})|, \quad (3)$$

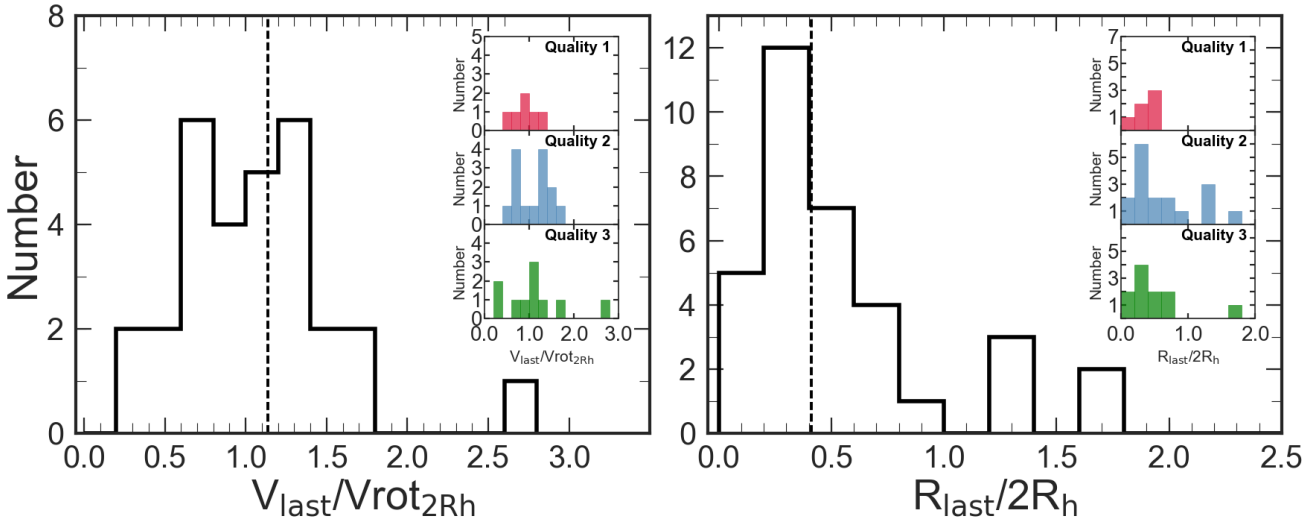

Figure 5. *Left:* Histogram of the ratio of the last rotational velocity data point to the velocity at $2R_h$. *Right:* Histogram of the ratio of the radius of the last data point on rotation curve to $2R_h$. Inset histograms show the distribution for the kinematic sub-classes (Section 3.10). Dashed line indicates the median in both figures, where $<R_{last}/2R_h> = 0.42 \pm 0.04$ and $<V_{last}/Vrot_{2R_h}> = 1.14 \pm 0.11$. On average extracting the rotational velocity at $2R_h$ requires extrapolation of the model beyond the last data point, leading to an decrease in velocity of $\sim 14\%$.

where Ψ takes values between 0° and 90°. In Figure 6 we show Ψ as a function of image axis ratio for the sample compared to the KROSS survey of $\sim$700 star-forming galaxies at $z \sim 0.8$. The sample covers a range of position angle misalignment, with $<\Psi> = 31.8^\circ \pm 5.7^\circ$, $10.52^\circ \pm 19.8^\circ$, $33.2^\circ \pm 15.2^\circ$ & $21.8^\circ \pm 17.5^\circ$ at $z = 0.84$, 1.47, 2.22 & 3.33 respectively. This is larger than that identified in KROSS at $z \sim 0.8$ (13°), but at all redshifts comparable to or within the criteria of $\Psi \leq 30^\circ$ imposed by Wisnioski et al. (2015), to define a galaxy as kinematically 'disky'. This indicates the average galaxy in our sample is on the boundary of what is considered to be a disk. A summary of the morphological properties for our sample is shown in Appendix C Table C1. Example broadband images of our sample are shown in the left panel of Figure 3, with the appropriate PA_{im} and integral field spectrograph field of view. The kinematic PA for the sample is derived in Section 3.4. We will use this criteria, together with other dynamical criteria later to define the most disk-like systems.

3.7 Two-dimensional Dynamical Modelling

To provide a parametric derivation and test of the numerical kinematic properties derived for each galaxy, we model the broadband continuum image and two-dimensional velocity field with a disk and halo model. The model is parametrised in the same way as the one-dimensional kinematic model used to interpolate the data points in each galaxies' rotation curve (Section 3.5) but takes advantage of the full two-dimensional extent of the galaxies velocity field. To fit the dynamical models to the observed images and velocity fields, we again use an MCMC algorithm. We first use the imaging data to estimate the size, position angle and inclination of the galaxy disk. Then using the best-fit parameter values from imaging as a first set of prior inputs to the code, we simultaneously fit the imaging and velocity fields. We allow the dynamical centre of the disk and position angle (PA_{vel}) to vary, but require that the imaging and dynamical centre to lie within 1 kpc (approximately the radius of a bulge at $z \sim 1$; Bruce et al. 2014). We note also that we allow the morphological and dynamical major axes to be independent. The routine converges when no further improvement in the reduced chi-squared of the fit can be achieved within 30 iterations. For a discussion of the model and fitting procedure see Swinbank et al. (2017).

For the sample of 34 galaxies the average of the ratio of kinematic positional angle derived from the velocity map to numerical modelling is $<PA_{vel(Slit)}/PA_{vel(2D)}> = 0.97 \pm 0.09$. Whilst the morphological position angle agree on average with $<PA_{im(Sérsic)}/PA_{im(2D)}> = 1.10 \pm 0.14$. We compare the velocity field generated from the fitting procedure, (see Figure 3 for examples), to the observed field for each galaxy derived from emission line fitting (Section 3.4). We derive a velocity error weighted rms based on the residual for each galaxy, and normalise this by the galaxies rotational velocity ($Vrot_{2R_h}$). On average the sample is well described by the disk and halo model, with the median rms of the residual images being $<rms> = 22 \pm 1.42$

3.8 Velocity Dispersions

To further classify the galaxy dynamics of our sources we also make measurements of the velocity dispersion of the star-forming gas (σ_0). High redshift star forming galaxies are typically highly turbulent clumpy systems, with non-uniform velocity dispersions (e.g. Genzel et al. 2006; Kassin et al. 2007; Stark et al. 2008; Förster Schreiber et al. 2009b; Jones et al. 2010; Johnson et al. 2018). The effects of beam smearing on our sample are reduced compared to non-AO observations due to the high AO-resolution although we still apply a correction. First we measure the velocity dispersion

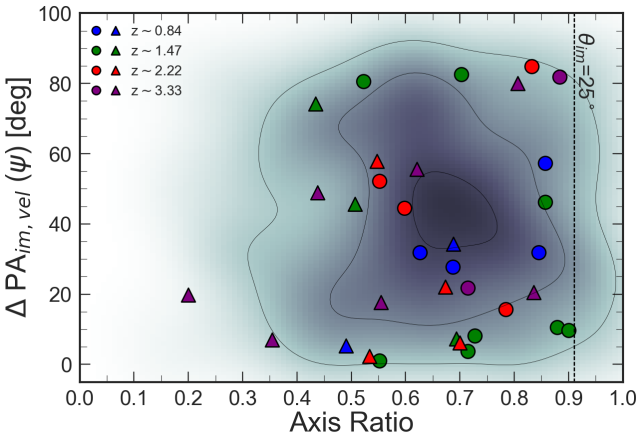

Figure 6. The absolute misalignment between the kinematic and morphological axes (Ψ) as a function of semi-minor(b) to semi-major(a) axis ratio for the galaxies in our sample derived from Sérsic fitting as a function of. Our sample is coloured by redshift as Figure 1, and the KMOS Redshift One Spectroscopic Survey (KROSS) is shown for comparison as the grey shaded region. The *circles* indicate galaxies with $\mathrm{Vrot}_{2\mathrm{R_h}}/\sigma_{\mathrm{median}} > 1$ whilst *triangles* highlight galaxies with $\mathrm{Vrot}_{2\mathrm{R_h}}/\sigma_{\mathrm{median}} < 1$. The majority of galaxies in our sample are moderately inclined with <b/a>=0.68 ±0.04 showing kinematic misalignment of Ψ <48°.

of each galaxy by taking the median of each velocity dispersion map, examples of which are shown in Figure 3, in an annulus between $\mathrm{R_h}$ and $2\mathrm{R_h}$. This minimises the effects of beam smearing towards the centre of the galaxy as well as the impact of low surface brightness regions in the outskirts of the galaxy. We also measure the velocity dispersion from the inner regions of the dispersion map as well as the map as a whole, finding excellent between all three quantities, to within on average 3%.

To take into account the impact of beam smearing on the velocity dispersion of the galaxies in our sample we follow the methods of Johnson et al. (2018). We measure the ratio of galaxy stellar continuum disk size ($\mathrm{R_d}$) to the half-light radii of the PSF of the AO observations deriving a median ratio of $< \mathrm{R_d} / \mathrm{R_h^{PSF}} > = 2.17 \pm 0.18$ which equates to an average velocity dispersion correction of ∼4%. We derive the correction for each galaxy in the sample and correct for beam smearing effects.

The average velocity dispersion for our sample is $< \sigma_{\mathrm{median}} > = 85 \pm 6\,\mathrm{km\,s^{-1}}$, with full range of $\sigma_{\mathrm{median}} = 40$–$314\,\mathrm{km\,s^{-1}}$. This is similar to KROSS at $z \sim 1$ which has $< \sigma_{\mathrm{median}} > = 83 \pm 2\,\mathrm{km\,s^{-1}}$ but much higher than the KMOS^{3D} survey which identified a decrease in the intrinsic velocity dispersion of star-forming galaxies by a factor of two from $50\,\mathrm{km\,s^{-1}}$ at $z \sim 2.3$ to $25\,\mathrm{km\,s^{-1}}$ at $z \sim 0.9$ (Wisnioski et al. 2015). The evolution of velocity dispersion with cosmic time is minimal in our sample with $< \sigma_{\mathrm{median}} > = 79 \pm 15\,\mathrm{km\,s^{-1}}$, $87 \pm 10\,\mathrm{km\,s^{-1}}$, $79 \pm 12\,\mathrm{km\,s^{-1}}$ & $83 \pm 27\,\mathrm{km\,s^{-1}}$ at $z = 0.84$, 1.47, 2.23 & 3.33 respectively. The KMOS Deep Survey (Turner et al. 2017) identified a stronger evolution in velocity dispersion with $\sigma_{\mathrm{int}} = 10$ - $20\,\mathrm{km\,s^{-1}}$ at $z \sim 0$, 30 - $60\,\mathrm{km\,s^{-1}}$ at $z \sim 1$ and 40 - $90\,\mathrm{km\,s^{-1}}$ at $z \sim 3$ in star-forming galaxies. This indicates that the lower redshift galaxies in our sample are more turbulent than the galaxy samples discussed in Turner et al. (2017). We note however, that the different selection functions of the observations will influence this result.

To measure whether the galaxies in our sample are 'dispersion dominated' or 'rotation dominated' we take the ratio of rotation velocity ($\mathrm{Vrot}_{2\mathrm{R_h}}$) to intrinsic velocity dispersion (σ_{median}), following Weiner et al. (2006); Genzel et al. (2006). Taking the full sample of 34 galaxies, we find a median ratio of rotational velocity to velocity dispersion, across all redshift slices of $< \mathrm{Vrot}_{2\mathrm{R_h}}/\sigma_{\mathrm{median}} > = 0.82 \pm 0.13$ with ∼32% having $\mathrm{Vrot}_{2\mathrm{R_h}}/\sigma_{\mathrm{median}} > 1$ (Figure 7). This is significantly lower than other high redshift IFU studies such as KROSS, in which 81% of its ∼600 star forming galaxies having $\mathrm{Vrot}_{2\mathrm{R_h}}/\sigma_0 > 1$ with a $< \mathrm{Vrot}_{2\mathrm{R_h}}/\sigma_0 > = 2.5 \pm 1.4$. We note that the median redshift of the KROSS sample is $< z > = 0.8$, compared to $< z > = 2.22$ for our sample. Johnson et al. (2018) identified that galaxies of stellar mass $10^{10}\mathrm{M_\odot}$ show a decrease in $\mathrm{Vrot}_{2\mathrm{R_h}}/\sigma_0$ from $z \sim 0$ to $z \sim 2$ by a factor ∼4.

The SINS/ZC-SINF AO survey of 35 star forming galaxies at $z \sim 2$ identify a median $\mathrm{V_{tot}}/\sigma_0 = 3.2$ ranging from $\mathrm{V_{tot}}/\sigma_0 = 0.97 - 13$ (Schreiber et al. 2018). In our sample at $z = 0.84$, 1.47, 2.23 & 3.33 the medain ratio is $< \mathrm{Vrot}_{2\mathrm{R_h}}/\sigma_{\mathrm{median}} > = 1.26 \pm 0.43$, 1.75 ± 0.90, 1.03 ± 0.20 & 0.52 ± 0.22 respectively. This indicates that on average the dynamics of the $z \sim 3.33$ galaxies in our sample are more dispersion driven. Turner et al. (2017) identified a similar result with KMOS Deep Survey galaxies at $z \sim 3.5$, finding a median value of $\mathrm{V_C}/\sigma_{\mathrm{int}} = 0.97 \pm 0.14$.

In order to compare our sample directly to other star-forming galaxy surveys we must remove the inherent scaling between stellar mass and V/σ, by mass normalising each comparison sample to a consistent stellar mass, for which we use $\mathrm{M_*} = 10^{10.5}\mathrm{M_\odot}$, following the procedures of Johnson et al. (2018). In Figure 7 we show the mass normalised V/σ of our sample as a function of redshift as well eight comparison samples taken from the literature. GHASP (Epinat et al. 2010; $z = 0.09$), SAMI (Bryant et al. 2015; $z = 0.17$), MASSIV (Epinat et al. 2012; $z = 1.25$), KROSS (Stott et al. 2016; $z = 0.90$), KMOS3D (Wisnioski et al. 2015; $z = 1$ & 2.20) SINS (Cresci et al. 2009; $z = 2.30$) and KDS (Turner et al. 2017; $z = 3.50$). We overplot tracks of $\mathrm{Vrot}_{2\mathrm{R_h}}/\sigma_{\mathrm{median}}$ as function of redshift, for different Toomre disk stability criterion ($\mathrm{Q_g}$; Toomre 1964) following the procedures of Johnson et al. (2018) and Turner et al. (2017), normalised to the median V/σ of the GHASP Survey at $z = 0.093$. The galaxies in our sample align well with the mass normalised comparison samples from the literature, with a trend of increasing V/σ with increasing cosmic time, as star-forming galaxies become more rotationally dominated.

3.9 Circular Velocities

It is well known that high redshift galaxies are highly turbulent systems with heightened velocity dispersions in comparison to galaxies in the local Universe. (e.g. Förster Schreiber et al. 2006, 2009b; Genzel et al. 2011; Swinbank et al. 2012a; Wisnioski et al. 2015). It is therefore necessary to account for the contribution of pressure support from turbulent motions to the circular velocity of high redshift galaxies. As shown in Burkert et al. (2016), if we assume the galaxies in our sample consist of an exponential disk with a radially

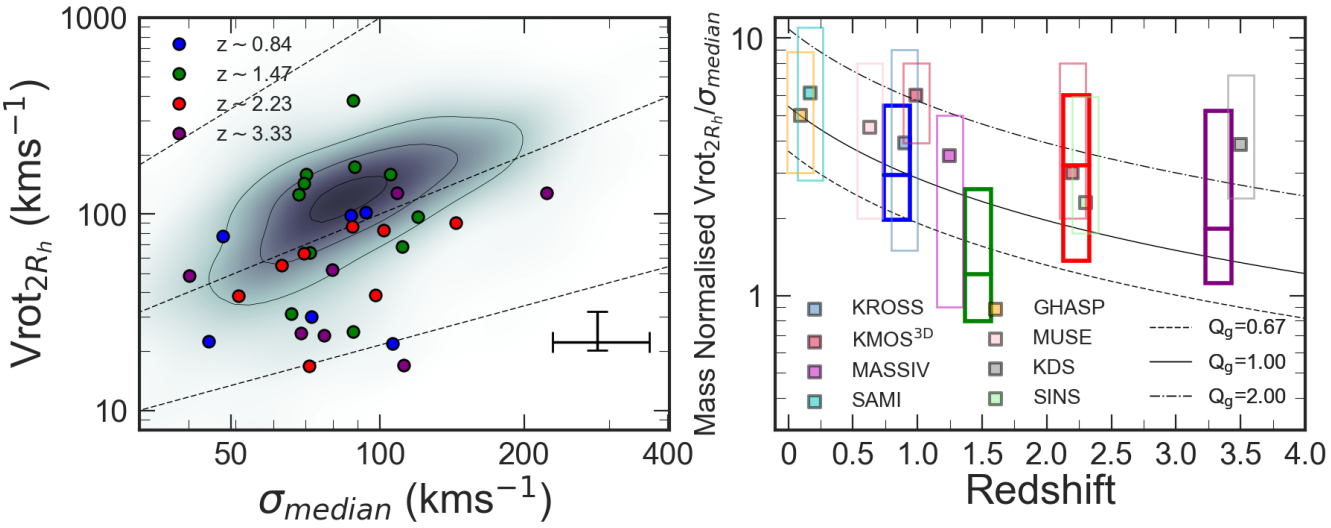

Figure 7. *Left*: Distribution of velocity $\mathrm{Vrot}_{2\mathrm{R_h}}$ and σ_{median} in our sample, coloured by spectroscopic redshift as in Figure 1. The KROSS $z\sim0.8$ survey is shown for comparison by the shaded region. Lines of $1.5\mathrm{Vrot}/\sigma_{\mathrm{median}}$, $\mathrm{Vrot}/\sigma_{\mathrm{median}}$ and $\mathrm{Vrot}/1.5\sigma_{\mathrm{median}}$ shown for reference. *Right*: Mass normalised $\mathrm{Vrot}_{2\mathrm{R_h}}/\sigma_{\mathrm{median}}$ as function of redshift, the 16th and 84th percentile shown by the extent of the box, median as a solid line at each redshift. We also show eight comparison surveys of star-forming galaxies from $0.09<z<3.5$ selected from the literature with median values shown by the squares. We plot tracks of $\mathrm{Vrot}_{2\mathrm{R_h}}/\sigma_{\mathrm{median}}$ as function of redshift, for different Toomre disk stability criterion ($\mathrm{Q_g}$; Toomre 1964) following the procedures of Johnson et al. (2018). The majority of the sample has a mass normalised $\mathrm{Vrot}_{2\mathrm{R_h}}/\sigma_{\mathrm{median}}>1$, with an indication of a slight evolution in the dominate dynamical support process with cosmic time, with $\mathrm{Vrot}_{2\mathrm{R_h}}/\sigma_{\mathrm{median}}$ increasing at lower redshift.

constant velocity dispersion, the true circular velocity of a galaxy ($\mathrm{V_{circ}(r)}$) is given by

$$\mathrm{V^2_{circ}(r)} = \mathrm{V^2_{rot}(r)} + 2\sigma_0^2(\frac{\mathrm{r}}{\mathrm{R_d}}), \quad (4)$$

where $\mathrm{R_d}$ is the disk scale length and σ_0 is the intrinsic velocity dispersion of the galaxy. For a galaxy with $\mathrm{V_{rot}}/\sigma_0 \geq 3$ the contribution from turbulent motions is negligible and $\mathrm{V_{circ}(r)} \approx \mathrm{V_{rot}(r)}$. All the galaxies in our sample have $\mathrm{V_{rot}}/\sigma_0 < 3$. For each object we convert the inclination corrected rotational velocity profile to a circular velocity profile. Following the same methods used to derive the rotational velocity of a galaxy (Section 3.5), we fit one dimensional dynamical models to the circular velocity profiles of each galaxy and extract the velocity at two times the stellar continuum half light radii of the galaxy ($\mathrm{V_{circ}(r=2R_h)}$). The ratio of $\mathrm{V_{circ}(r=2R_h)}$ to $\mathrm{V_{rot}(r=2R_h)}$ for each galaxy is shown in Appendix C Table C1. The median circular velocity to rotational velocity ratio for galaxies in our sample is $<\mathrm{V_{circ}(r=2R_h)/V_{rot}(r=2R_h)}>=3.15\pm0.41$ ranging from $\mathrm{V_{circ}(r=2R_h)/V_{rot}(r=2R_h)}=1.17-12.91$.

3.10 Sample Quality

Our sample of 34 star forming galaxies covers a broad range in rotation velocity and velocity dispersion. Figure 3 and Figure 7 demonstrate there is dynamical variance at each redshift slice, with a number of galaxies demonstrating more dispersion driven kinematics. To constrain the effects of these galaxies on our analysis, we define a sub–sample of galaxies with high signal to noise, rotation dominated kinematics and 'disky' morphologies.

We note that if we were to split the sample by galaxy integrated signal-to-noise rather than morpho-kinematic properties, we would not select 'disky' galaxies with rotation dominated kinematics as the best quality objects. Splitting the sample into three bins of signal to noise with S/N $\leq$ 14 (low), S/N > 14 & S/N $\leq$ 23 (medium) and S/N > 24 (high) we find 12, 11 and 11 galaxies in each bin respectively with the low and median S/N bins having a median redshift of $z=1.47\pm0.17$ and 1.45 ± 0.54 whilst the highest S/N bin has a median redshift of $z=2.24\pm0.38$. All three signal to noise bins and have median rotation velocities, velocity dispersion and specific angular momentum values within 1σ of each other, therefore not distinguishing between 'disky' rotation dominated galaxies and those with more dispersion driven dynamics.

The morpho-kinematic criteria that define our three sub–samples are;

- Quality 1: $\mathrm{Vrot}_{2\mathrm{R_h}}/\sigma_{\mathrm{median}}>1$ and $\Delta\mathrm{PA_{im,vel}}\Psi<30^\circ$
- Quality 2: $\mathrm{Vrot}_{2\mathrm{R_h}}/\sigma_{\mathrm{median}}>1$ or $\Delta\mathrm{PA_{im,vel}}\Psi<30^\circ$
- Quality 3: $\mathrm{Vrot}_{2\mathrm{R_h}}/\sigma_{\mathrm{median}}<1$ and $\Delta\mathrm{PA_{im,vel}}\Psi>30^\circ$

Of the 34 galaxies in the sample, 11 galaxies have $\mathrm{Vrot}_{2\mathrm{R_h}}/\sigma_{\mathrm{med}}>1$ and 17 have $\Delta\mathrm{PA_{im,vel}}\Psi<30^\circ$. We classify 6 galaxies that pass both criteria as 'Quality 1' whilst galaxies that pass either criteria are labelled 'Quality 2' (17 galaxies). The remaining 11 galaxies that do not pass either criteria are labelled 'Quality 3'.

The following analysis is carried out on the full sample of 34 galaxies as well as just the 'Quality 1 ' and 'Quality 2' galaxies. In general we draw the same conclusions from

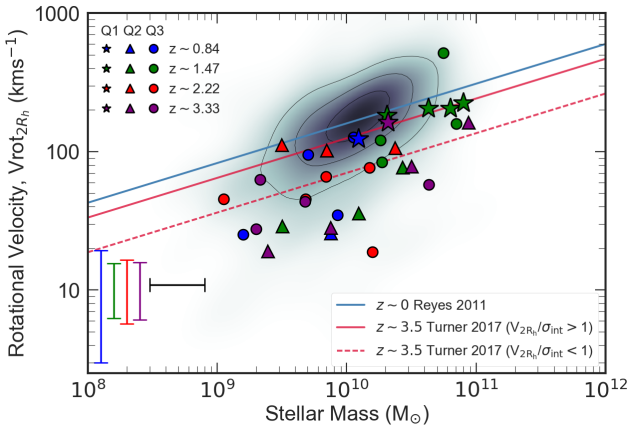

Figure 8. Rotation velocity extracted from the rotation curve at $2R_h$ as a function of stellar mass derived from SED fitting as described in Section 3, formally known as the Stellar Mass Tully Fisher relation. The sample is coloured by spectroscopic redshift, as in Figure 1, whilst the blue shaded region represents the KROSS $z\sim1$ sample (Harrison et al. (2017)). The *stars* represent 'Quality 1' targets ($Vrot_{2R_h}/\sigma_{med}>1$ and $\Delta PA_{im,vel}\Psi<30°$), *circles* 'Quality 2' ($Vrot_{2R_h}/\sigma_{med}>1$ or $\Delta PA_{im,vel}\Psi<30°$) and *triangles* 'Quality 3' galaxies ($Vrot_{2R_h}/\sigma_{med}<1$ and $\Delta PA_{im,vel}\Psi>30°$). We also show $z\sim0$ tracks from Reyes et al. (2011), $z\sim3.5$ tracks for rotation dominated ($Vrot_{2R_h}/\sigma_{int}>1$) and dispersion dominated ($Vrot_{2R_h}/\sigma_{int}<1$) galaxies in the KMOS Deep Survey (KDS) from Turner et al. (2017). There is a clear distinction between the different sub–samples, with 'Quality 1' galaxies having higher rotation velocity for a given stellar mass, aligning with the KROSS sample. 'Quality 3' targets have lower rotation velocities, aligning more with $Vrot_{2R_h}/\sigma_{int}<1$ KMOS Deep Survey $z\sim3.5$ track, whilst 'Quality 2' targets on average lie in between, with intermediate rotation velocities for a given stellar mass. The median uncertainty on rotational velocity at each redshift is shown in the lower left corner as well as the uncertainty of the stellar mass. The $z\sim1.47$ 'Quality 3' galaxy, with $Vrot_{2R_h}\sim380\,km\,s^{-1}$ has low inclination of $\sim25°$, hence large line-of-sight velocity correction.

the full sample as well the sub–samples, indicating the more turbulent galaxies in our sample do not bias our interpretations of the data. In each of the following sections we remark on the properties on 'Quality 1 ' and 'Quality 2' galaxies.

3.11 Rotational velocity versus stellar mass

The stellar mass 'Tully-Fisher relationship', (Figure 8), represents the correlation between the rotational velocity ($Vrot_{2R_h}$) and the stellar mass (M_*) of a galaxy (TFR; Tully & Fisher 1977, Bell & de Jong 2001). The relationship demonstrates the link between total mass (or 'dynamical mass')[2] of a galaxy, which can be probed by how rapidly the stars and gas are rotating, and the luminous (i.e. stellar) mass.

In Figure 8 we plot $Vrot_{2R_h}$ as a function of stellar mass for our sample as well as a sample of $z<0.1$ star-forming galaxies from Reyes et al. (2011) using spatially-resolved Hα kinematics. The KROSS survey at $z\sim1$ is also indicated (Harrison et al. 2017). We over plot two tracks from the KMOS Deep Survey (KDS; Turner et al. 2017), with median redshift of $z\sim3.5$. The KDS sample is split into 'rotation-dominated' systems ($Vrot_{2R_h}/\sigma_{int}>1$) and 'dispersion-dominated' systems ($Vrot_{2R_h}/\sigma_{int}<1$), for which we show both tracks.

Figure 8 shows a distinction between 'Quality 1' and 'Quality 2 / 3' galaxies. 'Quality 1' galaxies, which have the most disk-like properties have higher rotation velocity for a given stellar mass with a $<Vrot_{2R_h}>=151\,km\,s^{-1}\pm13\,km\,s^{-1}$, and align with the rotational velocities of the KROSS sample. The median rotation velocity of 'Quality 2 & 3' galaxies is $<V_{2R_h}>=53\,km\,s^{-1}\pm10\,km\,s^{-1}$, occupying similar parameter space to the $Vrot_{2R_h}/\sigma_{int}<1$ KMOS Deep Survey $z\sim3.5$ track. This is a consequence of construction, as 'Quality 1' galaxies have a median $<Vrot_{2R_h}/\sigma_{med}>=1.74\pm0.30$ whilst 'Quality 2 & 3' sources have $<Vrot_{2R_h}/\sigma_{med}>=0.62\pm0.11$

The Tully-Fisher relation provides a method to constrain galaxy dynamical masses however due to degeneracies and ambiguity in the evolution of the intercept and slope of the relationship with cosmic time (e.g. Übler et al. 2017; Tiley et al. 2018), and the strong implications of sample selection this becomes increasingly challenging. There is discrepancy amongst other high redshift star-forming galaxy studies (e.g. Conselice et al. 2005; Flores et al. 2006; Di Teodoro et al. 2016; Pelliccia et al. 2017) finding no evolution in the intercept or slope of Tully-Fisher relation. Even with the inclusion of non-circular motions through gas velocity dispersions via the kinematic estimator $S_{0.5}$ (e.g. Kassin et al. 2007; Gnerucci et al. 2011) no evolution across $\sim$8Gyr of cosmic time is found. Whilst other studies (e.g. Miller et al. 2012; Sobral et al. 2013b) identify evolution in the stellar mass zero point of $\Delta M^*=0.02\pm0.02$ dex out to $z=1.7$.

We have demonstrated that the galaxies in our sample exhibit properties that are typical for 'main sequence' star forming galaxies from $z=0.8-3.5$ and show good agreement with other high-redshift integral-field surveys when the sample selection is well matched (e.g. Übler et al. 2017; Harrison et al. 2017; Turner et al. 2017). For the remainder of this work we focus on a fundamental property of the galaxies in our sample; their angular momentum, which incorporates the observed velocity, galaxy size and stellar mass.

4 ANGULAR MOMENTUM

With a circular velocity, stellar mass and size derived for each galaxy, we can now turn our attention to analysing the angular momentum properties of our sample. First we investigate the galaxy stellar specific angular momentum of the disk. We then take advantage of the high resolution of the data, and study the distribution of angular momentum within each galaxy.

4.1 Total Angular Momentum

We start by deriving the stellar specific angular momentum (j_*=J_* / M_*) for the 34 star forming galaxies in our sample. This quantity, unlike other relations between stellar mass

[2] For rotationally-dominated galaxies Tiley et al. (2018)

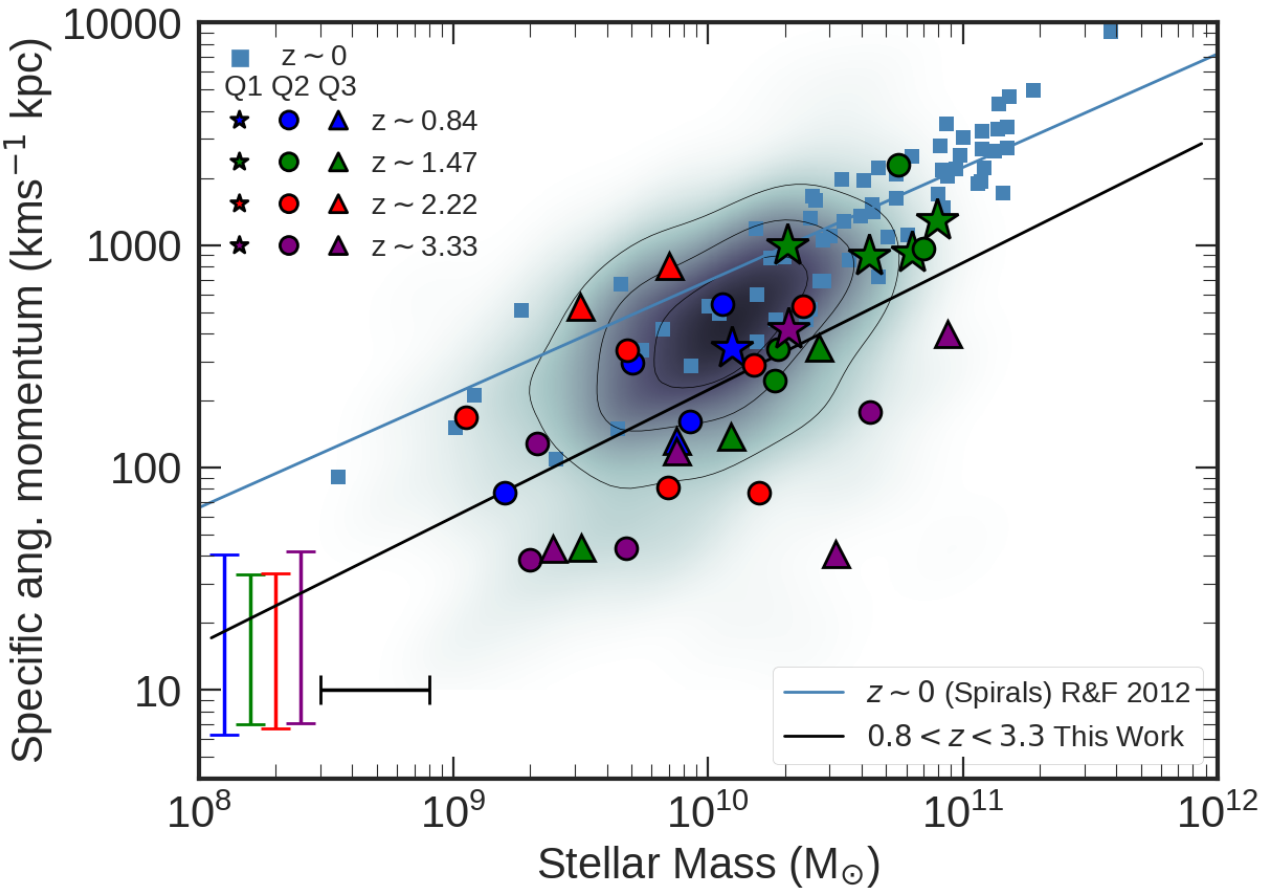

Figure 9. Specific stellar angular momentum as measured at $2R_h$ as a function of stellar mass. The sample coloured by spectroscopic redshift as as shown in Figure 1, and the blue shaded regions represents the KROSS $z\sim1$ sample (Harrison et al. 2017). The *stars* represent 'Quality 1' targets ($\mathrm{Vrot}_{2R_h}/\sigma_{\mathrm{med}}>1$ and $\Delta\mathrm{PA}_{\mathrm{im,vel}}\Psi<30°$), *circles* 'Quality 2' ($\mathrm{Vrot}_{2R_h}/\sigma_{\mathrm{med}}>1$ or $\Delta\mathrm{PA}_{\mathrm{im,vel}}\Psi<30°$) and *triangles* 'Quality 3' galaxies ($\mathrm{Vrot}_{2R_h}/\sigma_{\mathrm{med}}<1$ and $\Delta\mathrm{PA}_{\mathrm{im,vel}}\Psi>30°$). The $z\sim0$ Romanowsky & Fall (2012) comparison sample is shown, with the fit to the data of the form $\log_{10}(j_*)=\alpha+\beta(\log_{10}(M_*/M_\odot)-10.10)$, with $\alpha=2.89$ and $\beta=0.51$, whilst for KROSS ($z\sim1$) $\alpha=2.58$ and $\beta=0.62$. Our sample appears in good agreement with other $z\sim1$ samples, having lower specific stellar angular momentum for a given stellar mass than galaxies at $z\sim0$, with a $\alpha=2.41$ and $\beta=0.56$. The median uncertainty on specific angular momentum at each redshift is shown in the lower left corner as well as the uncertainty of the stellar mass.

and circular velocity, comprises of three uncorrelated variables with a mass scale and a length scale times a rotation-velocity scale (Fall & Efstathiou 1980, Fall 1983). The stellar specific angular momentum also removes the inherent scaling between total angular momentum and mass. It is derived from:

$$j_* = \frac{\mathrm{J}_*}{\mathrm{M}_*} = \frac{\int(\mathbf{r}\times\bar{\mathbf{v}}(r))\rho_*(r)\mathrm{d}^3\mathbf{r}}{\int\rho_*(r)\mathrm{d}^3\mathbf{r}}, \quad (5)$$

where $\mathbf{r}$ and $\bar{\mathbf{v}}$ are the position and mean-velocity vectors (with respect to the centre of mass of the galaxy) and $\rho(r)$ is the three dimensional density of the stars and gas (Romanowsky & Fall 2012).

In order to compare between observations and empirical models (or numerical models, as we will in Section 4.2.2), this expression can be simplified to be a function of intrinsic circular rotation velocity of the star forming gas and the stellar continuum half light radius. These intrinsic properties of the galaxy are correlated to the observable rotation velocity and disc scale length by the inclination of the galaxy and the PSF of the observations. As derived by Romanowsky & Fall (2012), this expression can be expanded to incorporate non-exponential disks. The specific angular momentum can be written as function of inclination and Sérsic index[3]:

$$j_* = k_\mathrm{n} C_\mathrm{i} v_\mathrm{s} R_\mathrm{h}, \quad (6)$$

Where v_s is the rotation velocity at $2\times$ the half-light radii (R_h), C_i is the correction factor for inclination, assumed to be $\sin^{-1}(\theta_{inc})$ (see Appendix A of Romanowsky & Fall 2012) and k_n is a numerical coefficient that depends on the Sérsic index, n, of the galaxy and is approximated as:

$$k_n = 1.15 + 0.029n + 0.062n^2, \quad (7)$$

We derive the specific stellar angular momentum of all 34

[3] See Romanowsky & Fall (2012) and Obreschkow & Glazebrook (2014) for the full derivation and discussion of this approach.

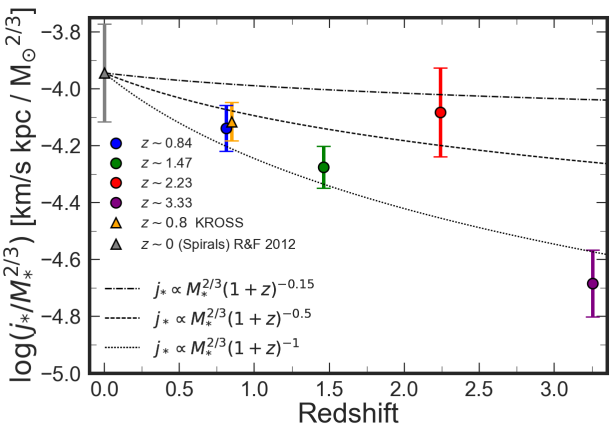

Figure 10. The redshift evolution of $j_*/M_*^{2/3}$ from $z\sim0$ to $z\sim3.3$. We show our sample coloured by redshift, as Figure 1 as well the $z=0$ disks from Romanowsky & Fall (2012) and the $z=0.8$ KROSS sample from Harrison et al. (2017). We overlay tracks of $j_*/M_*^{2/3}\propto(1+z)^{-n}$ with $n=0.15-1$ as derived in Obreschkow et al. (2015). Our galaxies show good agreement with other high redshift samples, and overall demonstrate a trend of decreasing $j_*/M_*^{2/3}$ with increasing redshift.

galaxies in our sample, adopting the appropriate Sérsic index for each galaxy as measured in Section 3.2, and for comparison we compare this to the specific angular momentum of the galaxies from the KROSS survey at $z\sim1$ (derived in the same way), as a function of stellar mass in Figure 9. We also show the specific angular momentum of $z\sim0$ disk galaxies from Romanowsky & Fall (2012). The full range of specific stellar angular momentum in the sample is $j_*=40-2200\,\mathrm{km\,s^{-1}kpc}$ with a median value of $<j_*>=294\pm70\mathrm{km\,s^{-1}kpc}$.

The $j_*-M_*/M_\odot$ relation can also be quantified by the relation $\log_{10}(j_*)=\alpha+\beta(\log_{10}(M_*/M_\odot)-10.10)$. For the $z\sim0$ sample, as derived in Romanowsky & Fall (2012), $\alpha=2.89$ and $\beta=0.51$. We fit the same model to our sample and derive $\alpha=2.41\pm0.05$ and $\beta=0.56\pm0.03$. This demonstrates that our sample has low specific angular momentum for a given stellar mass but with approximately the same dependence on stellar mass. This evolution in intercept was also identified in KROSS at $z\sim1$ with $\alpha=2.55$ and $\beta=0.62$ (Harrison et al. 2017).

We note however other integral field studies of high redshift star-forming galaxies such as Contini et al. (2016); Marasco et al. (2019) find no evolution in the intercept of the specifc stellar angular momentum stellar mass relation for high redshift galaxies. Both these studies model the integral field data in three dimensions using a model data cube. In addition Marasco et al. (2019) derive the specific stellar angular momentum of there sample directly from surface-brightness profiles of the galaxy as opposed to the approximations of angular momentum given in Equation 6.

One prediction of ΛCDM, is that the relation between the mass and angular momentum of dark matter haloes evolves with time (Mo et al. 1998). In a simple, spherically symmetric halo in a matter-dominated Universe, the specific angular momentum, $j_h=J_h/M_h$ should scale as $j_h=M_h^{2/3}(1+z)^{-1/2}$ and if the ratio of stellar-to-halo mass is independent of redshift, then the specific angular momentum of baryons should scale as $j_*\propto M_*^{2/3}(1+z)^{-1/2}$ (Behroozi et al. 2010; Munshi et al. 2013). At $z\sim3$ this simple model predicts that the specific angular momentum of disks should be a factor of ∼2 lower than at $z=0$. However, this 'closed box' model does not account for gas inflows or outflows, which can significantly affect the angular momentum of galaxy disks, with the redistribution of low angular momentum material from the central regions to the halo and the accretion of higher angular momentum material at the edges of the disk. This model further assumes the halo lies in a matter dominated Universe which only occurs at $z\gtrapprox1$. At lower redshifts the correlation is expected to be much weaker with $j_*\propto M_*^{2/3}(1+z)^{-0.15}$ (Catelan & Theuns 1996; Obreschkow et al. 2015). To search for this evolution in our sample, we derive $j_*/M_*^{2/3}$ at each redshift slice (Figure 10) and compare to the KROSS $z\sim0.8$ sample as well the Romanowsky & Fall (2012) disk sample at $z\sim0$. We find that galaxies in our sample between $z=0.8-3.33$ follow the scaling of $j_*/M_*^{2/3}\propto(1+z)^{-n}$ well, with lower specific angular momentum for a given stellar mass at higher redshift. Future work on larger non-AO samples of high-redshift star forming galaxies, such as the KMOS Galaxy Evolution Survey (KGES) will explore this correlation further (e.g. Gillman et al. in prep)

To understand the angular momentum evolution of the galaxies in our sample we can go beyond a measurement of size and asymptotic rotation speed, and take advantage of the resolved dynamics. Next we investigate how the radial distribution of angular momentum changes as a function of stellar mass and redshift to constrain how the internal distribution of angular momentum might affect the morphology of galaxies.

4.2 Radial Distribution of Angular Momentum

To quantify the angular momentum properties of the galaxies in our sample and to provide empirical constraints on the evolution of main sequence galaxies, from turbulent clumpy systems at high redshift with high velocity dispersion, to the well ordered 'Hubble' type galaxies seen in the local Universe, we can measure their internal dynamics. This is made possible with our adaptive optics sample of galaxies, with ∼kpc resolution integral field observations. In this section we discuss the method and show results for the construction of one dimensional radial angular momentum profiles of each galaxy.

We analyse the total stellar angular momentum distribution in the 'Quality 1 & 2' galaxies, galaxies with $\mathrm{Vrot}_{2R_h}/\sigma_{\mathrm{median}}>1$ or $\Delta\mathrm{PA}_{\mathrm{im,vel}}\Psi<30^\circ$ in our sample, as opposed to the specific stellar angular momentum in order to account for the evolution of the stellar mass distribution in galaxies with cosmic time. We focus on 'Quality 1 & 2' galaxies as these are the galaxies that most resemble star-forming kinematically stable 'rotationally supported' galaxies in our sample.

We infer how the angular momentum distribution changes by extracting the radius that encompasses 50% of the total (R_{J50}). We explore how this radius evolves as a function of redshift and to aid the interpretation compare them to fixed mass and evolving mass evolution tracks of

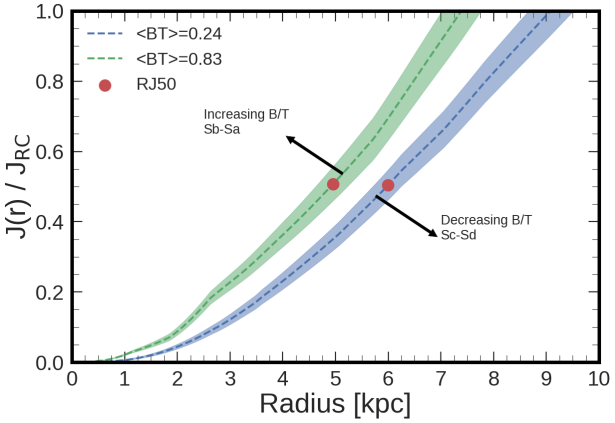

Figure 11. The total stellar angular momentum as a function of radius, normalised by the rotation curve estimate of the total angular momentum (Equation 6) for EAGLE galaxies with stellar mass $\log(10.5/M_{\odot})$ at $z = 0.1$. We define two sub-samples of galaxies using the B/T values defined in Trayford et al. (2018). We require $B/T > 0.6$, for a galaxy to be defined as bulge dominated, identifying a median B/T value for these galaxies of $< B/T > = 0.83$ which resemble Sb-Sa early-type galaxies. We also define a sample of disc-dominated galaxies, with the criteria $B/T < 0.4$. These galaxies align more with Sc-Sd late-type galaxies and have a median B/T value of $< B/T > = 0.24$. On average EAGLE galaxies of the same stellar mass, but with a more bulge-dominated morphologies have a smaller radii containing 50% of the angular momentum (R_{J50}).

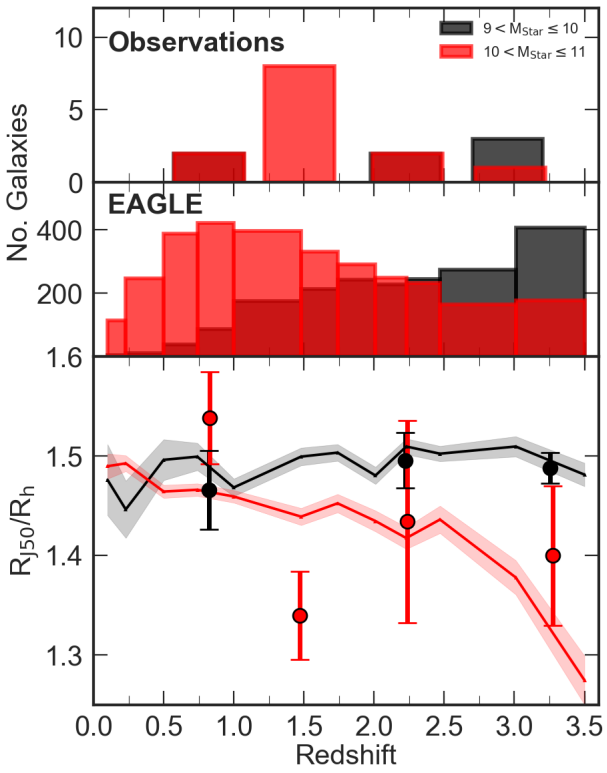

Figure 12. *Top*: The distributions of galaxies in each redshift slice for our sample and EAGLE. *Bottom:* The radius (R_{J50}) within which 50% of the galaxies angular momentum is contained, normalised by the half-light radius of the galaxy, as a function of redshift. Coloured points indicate the galaxies in our sample split into two stellar mass bins. The tracks show the median and 1σ evolution of EAGLE galaxies in the same redshift and stellar mass bins. R_{J50}/R_h in lower stellar mass galaxies shows no evolution with cosmic time whilst for higher mass galaxies a tentative evolution in the observational sample is seen. In EAGLE a similar trend is visible with higher stellar mass galaxies showing an increase in R_{J50}/R_h increasing by $\sim$16% from $z \sim 3.5$ to $z \sim 0.1$.

R_{J50} derived from a suitably selected sample of galaxies drawn from the EAGLE hydro-dynamical cosmological simulation from $0.1 \leq z \leq 3.5$ (Schaye et al. 2015a; Crain et al. 2015).

4.2.1 Angular Momentum Profile

We derive a stellar mass profile for each galaxy from the broadband photometry, as shown in Appendix B Table B1. We first construct a one dimensional surface brightness profile for each galaxy by placing elliptical apertures on the broadband photometry of the galaxy. We measure the surface brightness within each aperture (deconvolving the profile with the broadband PSF). We assume mass follows light, with the total stellar mass derived from the SED fitting, as for most objects with *HST* coverage we only have single band photometry and so are unable to measure (or include) mass to light gradients.

We use the circular velocity profiles as derived in Section 3.9, in order to account for the pressure support from the turbulent gas in the galaxies in our sample as well as to align more accurately with the dynamical rotation curves of the EAGLE galaxies (Section 4.2.2). We combine these with the stellar mass profiles. For each galaxy we measure the integrated stellar angular momentum as a function of radius J(r), which is then normalised against the total angular momentum estimate (Equation 6).

We then extract the radii at the which profile reaches 50% of its total. Since galaxy sizes also evolve with redshift (e.g. Roy et al. 2018), we normalise by the galaxies half light radius, in order to remove this intrinsic scaling. An example of the angular momentum profiles for a sample of EAGLE galaxies at $z \sim 0.1$ is shown in Figure 11.

To remove the implicit scaling between stellar mass and angular momentum distribution, we split the galaxies in our observed sample at each redshift slice in our sample into two stellar mass bins, $9 < \log(M_*[M_{\odot}]) \leq 10$ and $10 < \log(M_*[M_{\odot}]) \leq 11$. In Figure 12 we show how R_{J50} for both low and high stellar mass galaxies evolves with cosmic time. In the lowest stellar mass bin, the distribution of angular momentum remains constant whilst for the higher stellar mass galaxies ($10 < \log(M_*[M_{\odot}]) \leq 11$) there is a weak trend with redshift, with $< R_{J50z\sim3.5}/R_{J50z\sim0.84} > = 0.91 \pm 0.01$. If the radius which encloses 50% of the angular momentum in the galaxy has increased with cosmic time, relative to the size of the galaxy, this would suggest there is more angular momentum at larger radii in low redshift galaxies i.e the angular momentum in the galaxies has grown outwards with cosmic time.

In order to understand further the tentative trend that R_{J50}/R_h increases in galaxies with stellar mass $10 < \log(M_*[M_{\odot}]) \leq 11$ as suggested by our observational

sample, we make a direct comparison to the EAGLE hydrodynamical simulation which provides a significant comparison sample across a broad range of redshift.

4.2.2 EAGLE Comparison

To understand the context of the evolution of angular momentum in our sample we make a direct comparison to the Evolution and Assembly of GaLaxies and their Environments (EAGLE) hydrodynamical simulation (Schaye et al. 2015a; Crain et al. 2015).

The EAGLE simulation follows the evolution of dark matter, stars, gas and black holes in a 10^6 Mpc^3 cosmological volume from $z\sim10$ to $z\sim0$, recreating the local universe galaxy stellar mass function and colour-magnitude relations to high precision. It therefore provides a useful test bed to understand the observational biases and further interpret the angular momentum distributions in our galaxies.

Prior to making a comparison between the angular momentum properties of EAGLE galaxies and our observational sample, we first test the accuracy of using the EAGLE rotation curves as an estimate of the total angular momentum of the galaxy. The angular momentum of EAGLE galaxies can be derived directly from the sum of angular momentum of each star particle (J_{ps}) assigned to the galaxy, where:

$$J_{ps} = \sum_i m_i r_i \times v_i, \tag{8}$$

The rotation curves in EAGLE galaxies, as derived in Schaller et al. (2015), are generated by assuming circular motion for all bound material in a galaxies' halo. The simulated galaxies match the observations exceptionally well, both in terms of the shape and the normalisation of the curves, (for a full comparison to observations see Schaller et al. 2015; Schaye et al. 2015b).

In order to test whether our estimates of the total angular momentum from the rotation curves (J_{RC}) using Equation 6 are in good agreement with the particle angular momentum, we derive J_{RC} for each EAGLE galaxy using Equation 6 & 7 (with $n=1$).

In galaxies with high stellar particle angular momentum, J_{RC} on average accurately estimates the total angular momentum of the galaxy with $<J_{ps}/J_{rc}>=0.69\pm0.05$. We select galaxies in EAGLE where $J_{ps}<J_{RC}<2\times J_{ps}$ and adopt J_{ps} as the estimate of the total angular momentum of EAGLE galaxies.

4.2.3 Fixed Mass Evolution

To compare directly the angular momentum properties of EAGLE galaxies to our sample, we first match the selection function of the observations at each redshift snapshot in EAGLE. We select galaxies in EAGLE with stellar masses between $\log(M_*[M_\odot])=9-11$ and star formation rates $SFR[M_\odot yr^{-1}]=2-120$, which covers the range of our sample.

Following the same procedures as for the observations, we derive one-dimensional angular momentum profiles for each galaxy and measure R_{J50} (Figure 11). We do this for all EAGLE galaxies from $0.1\leq z\leq3.5$. We split the sample into the two stellar mass bins, applying the mass and star-formation selection of the observations at each redshift snapshot. In Figure 12 we plot median tracks of R_{J50} (normalised by the half stellar mass radius) as a function of redshift.

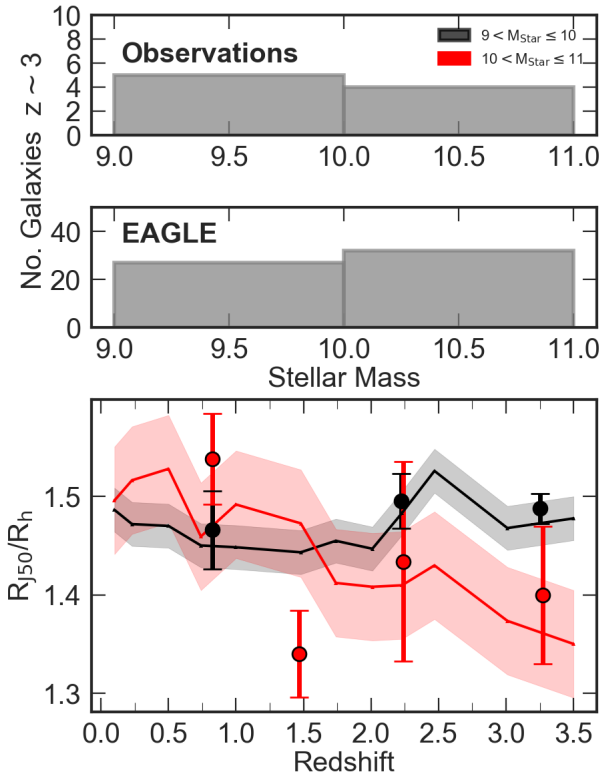

Figure 13. *Top*: The stellar mass distribution of our sample and EAGLE galaxies at $z=3$. *Bottom:* The radius (R_{J50}) within which 50% of the galaxies angular momentum is contained, normalised by the half-light radius of the galaxy as a function of redshift. Coloured points indicate the galaxies in our sample split into two stellar mass bins. The tracks show the median and 1σ evolution of EAGLE galaxies selected by stellar mass at $z=3$. For the EAGLE galaxies, we apply the stellar mass and star formation criteria at $z\sim3$ and trace the galaxies back to $z\sim0.1$ using the EAGLE merger trees, thus incorporating the mass evolution of galaxies. The galaxies in our sample have the mass criteria applied at their redshift and therefore shouldn't be compared directly to the tracks. We see similar evolution as the fixed mass tracks (Figure 12) with R_{J50}/R_h. increasing by ∼11% from $z\sim3.5$ to $z\sim0.1$. and minimal evolution in the lower stellar mass galaxies.

The evolution of EAGLE galaxies angular momentum distribution agrees well with the evolution in our sample. EAGLE predicts little evolution in the lowest stellar mass bin, with R_{J50} remaining approximately constant from $z=3.5$ to $z=0.1$. The higher stellar mass galaxies show an evolution from $R_{J50\,z\sim3.5}=1.27\pm0.02$ to $R_{J50\,z\sim0.1}=1.48\pm0.01$, an increase of ∼16%. The distribution of angular momentum in high stellar mass galaxies is growing outwards with increasing cosmic time. A galaxy of stellar mass $10^{10.5}M_\odot$ at $z=3.5$ will have a more concentrated angular momentum distribution, normalised to its half-light radius, than a $10^{10.5}M_\odot$ galaxy at $z=0.1$. This evolution in the angular momentum distribution could be driven by a number of physical processes. The accretion of high angular momen-

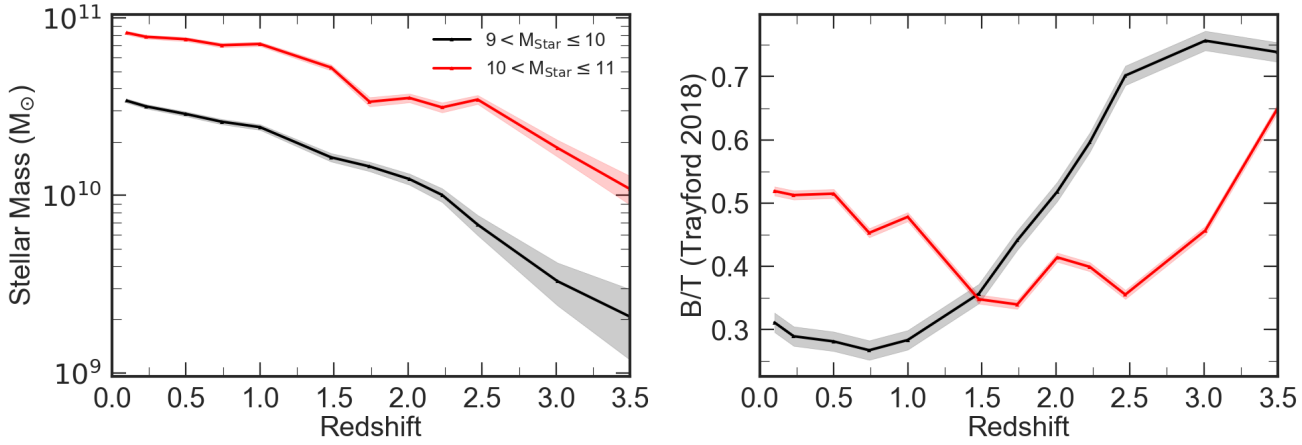

Figure 14. The stellar mass (*Left*) and bulge-total fraction (*Right*) as a function of redshift for EAGLE galaxies selected at $z=3$ with $\log(M_*[M_\odot])=9-11$ and star formation rates $SFR[M_\odot yr^{-1}]=2-120$. We split the galaxies into stellar mass bins of $9<\log(M_*[M_\odot])\leq10$ and $10<\log(M_*[M_\odot])\leq11$. Both stellar bins show comparable evolution in stellar mass with redshift. The B/T values for galaxies with stellar mass between $10<\log(M_*[M_\odot])\leq11$ indicate the formation pseudo-bulges at $z<1.5$ compared to $9<\log(M_*[M_\odot])\leq10$ stellar mass galaxies which continue to maintain there bulge-total fractions beyond $z<1.0$

tum material to the outer regions of the galactic disk which would act to increase the total angular momentum and thus R_{J50} of the galaxy.

Over the cosmic time between $z=3$ and $z=0.1$ (~10 Gyr) galaxies grow in stellar mass (e.g. Baldry et al. 2012; Behroozi et al. 2013; Furlong et al. 2015; Roy et al. 2018). Based on the EAGLE simulation (Crain et al. 2015; Schaye et al. 2015b), a galaxy in our $z=3$ sample would grow by a factor ~10 in stellar mass (factor of ~3 for a $z=2$ galaxy and a factor of ~1.5 for a $z=1$ galaxy). The gain in stellar mass dominates the stellar mass that is in place at higher redshift. Thus we expect the changes in galaxy angular momentum and its distribution arise primarily from the accretion of new star forming gas. As the angular momentum of the in-falling gas grows with time, the recently formed stellar population will have a higher angular momentum compared to the total stellar population. (e.g. Catelan & Theuns 1996; Obreschkow et al. 2015).

The removal of low angular momentum material via nucleated outflows driven by stellar winds would redistribute the angular momentum in the galaxy. If the evolution of angular momentum is being driven by nucleated outflows from across the galactic disk, we expect a similar increase in R_{J50} with low angular momentum material being removed. In-situ bulge formation at the centre of galaxies, increasing the fraction of low angular momentum material would alter the angular momentum profile of the galaxy. We note that we are studying the angular momentum evolution of star-forming gas associated with young massive stars. The older stars may have their orbit perturbed over time to form the galaxy's bulge. This complicates the interpretation of R_{J50}/R_h, but leads to a model in which the stellar bulge-to-total (B/T) ratio of the galaxy may be an effective measure of its past to current star formation rate. Recently, Wang et al. (2018) identified that the impact of bulge formation on a galaxies angular momentum distribution depends on the significance of the bulge, with very high B/T galaxies maintaining their original angular momentum distribution.

It is important to remember, however, that the galaxy sample we identify at higher redshift does not evolve into the galaxy sample at $z=0$. Many of the $z=3$ galaxies with stellar masses $\sim10^{10.5}M_\odot$ are likely to be $\sim10^{11}M_\odot$ at $z\sim0$ and will evolve into passive elliptical galaxies, perhaps at the centres of galaxy groups. These galaxies may become passive due to the the impact of black holes (e.g. Bower et al. 2006, 2017; Davies et al. 2018). Other galaxies may merge with larger central group galaxies and disappear from observational samples entirely. A galaxy of stellar mass $\sim10^{9.5}M_\odot$ at $z\sim3$ is likely to be $\sim10^{10}M_\odot$ at $z\sim0$ and thus more likely to evolve into late-type 'disc' galaxy at low-redshift. Instead of the observations tracing individual galaxies, we are viewing a sequence of snap shots of the star forming population at each epoch, and exploring how the angular momentum evolves in this sense.

The selection function used in observations and EAGLE comparison from $z=3.5-0.1$ for the radii derived in Figure 12 are not selecting the same descendent populations. To understand whether the evolution of R_{J50} is driven by the accretion of new material or bulge formation, we need to study the galaxies as they evolve. EAGLE allows us to follow the evolution of individual galaxies through cosmic time, which is what we now finally focus on.

4.2.4 Evolving Mass Evolution

One of the main advantages of a hydro-dynamical simulation is having the ability to trace the evolution of individual galaxies across cosmic time. The mass evolution of a given galaxy can be traced as it evolves via secular processes and interactions with other galaxies. This is achieved using the merger trees output by the simulation (McAlpine et al. 2016; Qu et al. 2017). We can use this information to derive the evolution of R_{J50} from $z=3.5$ to $z=0.1$ in individual EAGLE galaxies selected at high redshift.

We derive the radius containing fifty percent of the galaxies angular momentum (R_{J50}) for galaxies with

$\log(M_*[M_\odot]) = 9-11$ and $SFR \geq 2\,M_\odot yr^{-1}$ at $z = 3$. In Figure 13 we show the evolution of R_{J50} for these galaxies split into the two stellar mass bins at $z \sim 3$ as well as our observational sample for reference. We note the data points should not be directly compared to the EAGLE tracks due to differences in selection. The higher stellar mass EAGLE galaxies in Figure 13 show evolution in R_{J50} with $R_{J50\,z\sim3.5} = 1.23 \pm 0.05$ to $R_{J50\,z\sim0.1} = 1.37 \pm 0.03$, an increase of ∼11%. The evolution of angular momentum, quantified by R_{J50}, in EAGLE galaxies with $\log(M_*[M_\odot]) = 9-11$ and $SFR[M_\odot yr^{-1}] = 2-120$ at $z = 3$, increases with cosmic time. The angular momentum in these galaxies is becoming less centrally concentrated as the galaxy evolves, as indicated in Figure 12.

To understand the physical processes driving the increase R_{J50} relative to half-light radius of higher stellar mass galaxies, we analyse the stellar mass growth and evolution of stellar bulge-total (B/T) fraction in these galaxies (Figure 14). The stellar mass of the galaxy is extracted at each redshift snapshot in the EAGLE simulation. The bulge-to-total ratios are taken from Trayford et al. (2018), where the disk fraction of the galaxy is defined as the prograde excess (the mass in co-rotation above what would be expected for a purely pressure-supported system) and the B/T is the complement of this.

In EAGLE star-forming galaxies with stellar mass between $10 < \log(M_*[M_\odot]) \leq 11$ at $z = 3.5$ have significant bulge fractions; $B/T = 0.65 \pm 0.08$. As the galaxies evolve with cosmic time their stellar mass grows through accretion of new material from the surrounding circumgalactic medium, increasing by a factor ∼5 by $z = 1.5$. Their bulge fractions reduce to $B/T = 0.35 \pm 0.04$ at $z = 1.5$ and the radius containing 50% of their stellar angular momentum (R_{J50}) has increased by a ∼7% relative to their half-stellar mass radius in this period, indicating the presence of a more significant disk component in this galaxies from the recently accreted higher angular momentum material. Below $z = 1.5$ the high stellar mass galaxies continue to accrete more material and the angular momentum continues to grow outwards with cosmic time, with R_{J50}/R_h increasing by just ∼4% from $z = 1.5$ to $z = 0$. The bulge fraction below $z = 1.5$ however, begins to increase as these galaxies are massive enough to form pseudo-bulges, and resemble more Sa-Sb early-type morphologies.

For lower stellar mass star-forming galaxies in EAGLE with $9 < \log(M_*[M_\odot]) \leq 10$ the distribution of stellar angular momentum remains roughly constant relative to the half stellar mass radius of the galaxies from $z = 3.5$ to $z = 0$. In this period however the galaxies stellar mass has increased by a factor of ∼10 and the bulge fraction of the galaxies has significantly reduced from $B/T = 0.74 \pm 0.04$ at $z = 3.5$ to $B/T = 0.28 \pm 0.03$ at $z = 1$. From $z = 1$ to $z = 0$ the bulge-fraction of the galaxies remains relatively constant. This indicates at high-redshift these lower stellar mass galaxies are compact and spheroidal and as they evolve they accrete new material from the circumgalactic medium which builds the disc-component of the galaxy driving them towards Sd-Sc late-type morphologies. Below $z = 1$ the galaxies 'settle' becoming more stable and maintain an approximately constant bulge-fraction.

5 CONCLUSIONS

We have presented Hα and [OIII] adaptive optics integral field observations of 34 star forming galaxies from $0.8 \leq z \leq 3.3$ observed using the NIFS, SINFONI and OSIRIS spectrographs. The sample has a median redshift of $< z > = 2.22$, and covers a range of stellar masses from $\log(M_*[M_\odot]) = 9.0-10.9$, with 'main-sequence' representative star formation rates of $SFR_{H\alpha} = 2-120\ M_\odot yr^{-1}$. Our findings are summarised as follows:

- For 21 galaxies in our sample we measure continuum half light sizes using *HST* photometry and ground based broad-band imaging from the parametric fitting of a single Sérsic model. We find $< R_h^G / R_h^{HST} > = 0.97 \pm 0.05$ (Figure 2). Applying the same fitting procedure to remainder of the sample we derive $< R_h > = 0\farcs40 \pm 0\farcs06$, ∼4kpc at the median redshift of the sample. We conclude the continuum sizes of the galaxies in our sample are comparable to other high-redshift star-forming galaxies such as those presented in Stott et al. (2013); van der Wel et al. (2014).
- We identify that 11 (∼32%) of the galaxies in our sample have dynamics indicating they are supported by rotational gas kinematics, with rotational velocities that are of order the intrinsic velocity dispersion. We measure a median $< Vrot_{2R_h} / \sigma_{median} > = 0.82 \pm 0.13$ for the sample (Figure 7). We compare the mass normalised V/σ for our sample to other star-forming galaxy surveys, across a range of redshift, identifying our sample follows a similar trend of increasing in V/σ with cosmic time, as galaxies becomes more rotationally dominated.
- We place our sample in the context of other integral field studies by exploring the relation between rotational velocity and stellar mass (Figure 8). We identify no significant evolution in the relation since $z \sim 0$. Our galaxies are consistent with the dispersion dominated KMOS Deep Survey at $z \sim 3.5$; Turner et al. (2017) and other high-redshift surveys such as KROSS Tiley et al. (2018) and KMOS^{3D} Übler et al. (2018).
- We combine the inclination-corrected rotational velocities, half light sizes and stellar masses, to investigate how the relationship between specific stellar angular momentum and stellar mass in our sample evolves with cosmic time (Figure 9). We quantify the $j_* - M_*$ correlation with $\log(j) = \alpha + \beta(\log(M) - 10.10)$, finding $\alpha = 2.41 \pm 0.05$ and $\beta = 0.56 \pm 0.03$. The normalisation of the $j_* - M_*$ relation for our sample is smaller than other (non-AO) samples at $z \sim 1$ and $z \sim 0$ spiral galaxies. We derive the evolution of $j_*/M_*^{2/3} \propto (1+z)^{-n}$ for our sample (Figure 10) identifying that the galaxies in our sample agree well with the prediction of ΛCDM with $n = 0.5-1$.
- Taking advantage of the ∼kpc resolution of our observations we investigate the radial distribution of angular momentum in each galaxy, deriving one-dimensional stellar angular momentum profiles. We quantify these profiles by the 50% radii (R_{J50}) and explore their median evolution with cosmic time for galaxies with stellar mass in the range $9 < \log(M_*[M_\odot]) \leq 10$ and $10 < \log(M_*[M_\odot]) \leq 11$. We identify in the higher stellar mass bin a tentative trend of increasing R_{J50}/R_h with cosmic time (Figure 12).
- We note however the analysis we have undertaken on a sample of high redshift star-forming galaxies is limited by assumptions we have made. Throughout the analysis we

assumed our galaxies resemble kinematically well behaved 'discs' and that the sample is representative of the high redshift population. However it is well known that peculiar galaxies become the dominant morphological population at higher redshift with galaxies having much higher velocity dispersions comparable to the their rotational component. We therefore rely on hydrodynamical simulations to verify the conclusions we have drawn from the data.

- To confirm the trend of R_{J50}/R_h in higher stellar mass galaxies increasing with cosmic time we make a direct comparison to the Evolution and Assembly of GaLaxies and their Environments (EAGLE) hydro-dynamical simulation. We first test the validity of using the EAGLE rotation curves as derived in Schaller et al. (2015) to estimate the stellar angular momentum of EAGLE galaxies. We find good agreement between J_{RC} as derived from Equation 7 and the stellar particle angular momentum (J_{ps}) suggesting that EAGLE rotation curves can be used to accurately estimate the angular momentum of EAGLE galaxies.
- To compare to the observational sample we select galaxies in EAGLE by mass and star formation rate that match the selection function of the observations. One-dimensional stellar angular momentum profiles are derived for each EAGLE galaxy from which we measured the 50% angular momentum radii (R_{J50}). Splitting the EAGLE sample into two stellar mass bins of $9 < \log(M_*[M_\odot]) \leq 10$ and $10 < \log(M_*[M_\odot]) \leq 11$, we identify a 16% increase in R_{J50}/R_h from $z = 3.5$ to $z = 0.1$ in higher stellar mass galaxies and minimal evolution in the lower stellar mass bin, as identified in the observations (Figure 12).
- We note however that the selection function used in observations and EAGLE comparison from $z = 3.5$ to $z = 0.1$ for the radii derived in Figure 12 are not selecting the same descendent populations. To understand how a galaxies angular momentum distribution evolves with cosmic time we need to study galaxies as they evolve. Using the merger trees in EAGLE we select galaxies at $z = 3$ that match the selection function of our observations, and trace these galaxies through the simulation to $z = 0.1$, measuring the radius containing 50% of the stellar angular momentum (R_{J50}) at each redshift snapshot (Figure 13). Splitting the sample into the two stellar mass bins, we identify an 11% increase in R_{J50}/R_h from $z = 3.5$ to $z = 0.1$ in higher stellar mass galaxies.
- To understand the physical processes driving the increase in R_{J50}/R_h in higher stellar mass galaxies we explore the evolution of the stellar mass and bulge-fraction as a function of cosmic time (Figure 14). Both high and low stellar mass galaxies show an increase in stellar mass by a factor of $\sim$10 from $z = 3.5$ to $z = 0.1$. The bulge fraction of galaxies with stellar mass $9 < \log(M_*[M_\odot]) \leq 10$, decreases from $B/T = 0.74 \pm 0.04$ at $z = 3.5$ to $B/T = 0.28 \pm 0.03$ at $z = 1$, remaining roughly constant to $z = 0.1$. Higher stellar mass galaxies, those with stellar masses in the $10 < \log(M_*[M_\odot]) \leq 11$ at $z = 3$, show a decrease in bulge fraction from $B/T = 0.65 \pm 0.08$ at $z = 3.5$ to $B/T = 0.35 \pm 0.04$ at $z = 1.5$, but with an increase below $z = 1.5$ to $B/T = 0.53 \pm 0.03$ at $z = 0.1$. The accretion of new material from the circumgalactic medium reduces the bulge-fraction of both low and high stellar mass galaxies as they evolve with cosmic time. Below $z = 1$ the low mass galaxies become stable with approximately constant bulge fractions and Sc-Sd late morphologies, whilst the higher stellar mass galaxies continue to increase their bulge fraction through the formation of pseudo bulges leading to more early-type morphologies.

Overall our results show that high stellar mass main sequence star forming galaxies have a stronger evolution in angular momentum compared to low stellar mass galaxies. This process is likely to be driven by an internal redistribution of angular momentum from the accretion of new higher angular momentum material as well as other less dominant secular processes leading to the formation of pseudo-bulges. It is this process of redistributing the angular momentum, that coincides with changes in the galaxies morphology driving the galaxies towards the stable low-redshift disks that occupy the Hubble Sequence.

ACKNOWLEDGEMENTS

We thank the anonymous referee for their comments and suggestions, which improved the content and clarity of the paper. This work was supported by the Science and Technology Facilities Council (ST/L00075X/1). SG acknowledge the support of the Science and Technology Facilities Council through grant ST/N50404X/1 for support. IRS acknowledge support from STFC (ST/P000541/1) and the ERC Advanced Grant DUSTYGAL (321334). E.I. acknowledges partial support from FONDECYT through grant N° 1171710. JEG thanks the Royal Society for support via a University Research Fellowship. PNB is grateful for support from STFC via grants ST/M001229/1 and ST/R000972/1. ALT acknowledges support from STFC (ST/P000541/1) and ERC Advanced Grant DUSTYGAL (321334). J. M. acknowledges the support given by CONICYT Chile (CONICYT-PCHA/Doctorado-Nacional/2014-21140483).

REFERENCES

Abraham R. G., van den Bergh S., 2001, Science, 293, 1273
Almaini O., et al., 2007, in Metcalfe N., Shanks T., eds, ASP Conference Series Vol. 379, Cosmic Frontiers. p. 163
Aquino-Ortíz E., et al., 2018, MNRAS, 479, 2133
Baena Gallé R., Gladysz S., 2011, PASP, 123, 865
Baldry I. K., et al., 2012, MNRAS, 421, 621
Behroozi P. S., Conroy C., Wechsler R. H., 2010, ApJ, 717, 379
Behroozi P. S., Wechsler R. H., Conroy C., 2013, ApJ, 770, 57
Bell E. F., de Jong R. S., 2001, ApJ, 550, 212
Bertola F., Capaccioli M., 1975, ApJ, 200, 439
Best P., et al., 2013, in Thirty Years of Astronomical Discovery with UKIRT. Springer Netherlands, Dordrecht, pp 235–250
Bonnet H., et al., 2004a, The Messenger, 117, 17
Bonnet H., et al., 2004b, The Messenger, 117, 17
Bournaud F., et al., 2008, A&A, 486, 741
Bower R. G., Benson A. J., Malbon R., Helly J. C., Frenk C. S., Baugh C. M., Cole S., Lacey C. G., 2006, MNRAS, 370, 645
Bower R. G., Schaye J., Frenk C. S., Theuns T., Schaller M., Crain R. A., McAlpine S., 2017, MNRAS, 465, 32
Bruce V. A., et al., 2014, MNRAS, 444, 1660
Bryant J. J., et al., 2015, MNRAS, 447, 2857
Burkert A., 2009, in Jogee S., Marinova I., Hao L., Blanc G. A., eds, Vol. 419, Galaxy Evolution: Emerging Insights and Future Challenges. p. 3
Burkert A., et al., 2016, ApJ, 826, 214

Calzetti D., Armus L., Bohlin R. C., Kinney A. L., Koornneef J., Storchi-Bergmann T., 2000, ApJ, 533, 682
Catelan P., Theuns T., 1996, MNRAS, 282, 436
Chabrier G., 2003, PASP, 115, 763
Circosta C., et al., 2018, arXiv e-prints, p. arXiv:1809.04858
Cochrane R. K., Best P. N., Sobral D., Smail I., Geach J. E., Stott J. P., Wake D. A., 2018, MNRAS, 475, 3730
Conselice C. J., Gallagher III J. S., Wyse R. F. G., 2002, AJ, 123, 2246
Conselice C. J., Bundy K., Ellis R. S., Brichmann J., Vogt N. P., Phillips A. C., 2005, ApJ, 628, 160
Conselice C. J., Bluck A. F. L., Ravindranath S., Mortlock A., Koekemoer A. M., Buitrago F., Grützbauch R., Penny S. J., 2011, MNRAS, 417, 2770
Contini T., et al., 2016, A&A, 591, A49
Cortese L., et al., 2016, MNRAS, 463, 170
Crain R. A., et al., 2015, MNRAS, 450, 1937
Cresci G., Davies R. I., Baker A. J., Mannucci F., Lehnert M. D., 2007, in Afonso J., Ferguson H. C., Mobasher B., Norris R., eds, ASP Conference Series Vol. 380, Deepest Astronomical Surveys. p. 503
Cresci G., et al., 2009, ApJ, 697, 115
Davies R. I., 2007, MNRAS, 375, 1099
Davies J. J., Crain R. A., McCarthy I. G., Oppenheimer B. D., Schaye J., Schaller M., McAlpine S., 2018, preprint, (arXiv:1810.07696)
Delgado-Serrano R., Hammer F., Yang Y. B., Puech M., Flores H., Rodrigues M., 2010, A&A, 509, A78
Di Teodoro E. M., Fraternali F., Miller S. H., 2016, A&A, 594, A77
Eales S. A., et al., 2018, MNRAS, 481, 1183
Elmegreen D. M., et al., 2014, ApJ, 787, L15
Elson E. C., 2017, MNRAS, 472, 4551
Epinat B., Amram P., Balkowski C., Marcelin M., 2010, MNRAS, 401, 2113
Epinat B., et al., 2012, A&A, 539, A92
Exposito J., Gratadour D., Clénet Y., Rousset G., Mugnier L., 2012, in Adaptive Optics Systems III. p. 84475X
Fall S. M., 1983, in Athanassoula E., ed., IAU Symposium Vol. 100, Internal Kinematics and Dynamics of Galaxies. pp 391–398
Fall S. M., Efstathiou G., 1980, MNRAS, 193, 189
Fall S. M., Romanowsky A. J., 2018, ApJ, 868, 133
Ferguson H. C., et al., 2004, in American Astronomical Society Meeting Abstracts. p. 1449
Flores H., Hammer F., Puech M., 2006, New Astronomy Reviews, 50, 430
Foreman-Mackey D., Hogg D. W., Lang D., Goodman J., 2013, PASP, 125, 306
Förster Schreiber N. M., et al., 2006, ApJ, 645, 1062
Förster Schreiber N. M., et al., 2009b, ApJ, 706, 1364
Förster Schreiber N. M., et al., 2009a, ApJ, 706, 1364
Förster Schreiber N. M., Shapley A. E., Erb D. K., Genzel R., Steidel C. C., Bouché N., Cresci G., Davies R., 2011a, ApJ, 731, 65
Förster Schreiber N. M., et al., 2011b, ApJ, 739, 45
Förster Schreiber N. M., et al., 2014, ApJ, 787, 38
Freeman K. C., 1970, ApJ, 160, 811
Furlong M., et al., 2015, MNRAS, 450, 4486
García Marín M., et al., 2018, in Society of Photo-Optical Instrumentation Engineers (SPIE) Conference Series. p. 107041I
Geach J. E., Smail I., Best P. N., Kurk J., Casali M., Ivison R. J., Coppin K., 2008, MNRAS, 388, 1473
Genzel R., et al., 2006, Nature, 442, 786
Genzel R., et al., 2011, ApJ, 733, 101
Gnerucci A., et al., 2011, A&A, 528, A88
Harrison C. M., et al., 2017, preprint, (arXiv:1701.05561)
Hoyle F., 1956, Vistas in Astronomy, 2, 1702
Hubble E. P., 1926, ApJ, 64, 321
Johnson H. L., et al., 2018, MNRAS, 474, 5076
Jones T. A., Swinbank A. M., Ellis R. S., Richard J., Stark D. P., 2010, MNRAS, 404, 1247
Kassin S. A., et al., 2007, ApJ, 660, L35
Kauffmann G., et al., 2003, MNRAS, 341, 33
Khostovan A. A., Sobral D., Mobasher B., Best P. N., Smail I., Stott J. P., Hemmati S., Nayyeri H., 2015, MNRAS, 452, 3948
Lagos C. d. P., Theuns T., Stevens A. R. H., Cortese L., Padilla N. D., Davis T. A., Contreras S., Croton D., 2017, MNRAS, 464, 3850
Larkin J., et al., 2006, in Society of Photo-Optical Instrumentation Engineers (SPIE) Conference Series. p. 62691A
Lawrence A., et al., 2007, MNRAS, 379, 1599
Livermore R. C., et al., 2012, MNRAS, 427, 688
Livermore R. C., et al., 2015, MNRAS, 450, 1812
Marasco A., Fraternali F., Posti L., Ijtsma M., Di Teodoro E. M., Oosterloo T., 2019, A&A, 621, L6
Markwardt C. B., 2009, in Bohlender D. A., Durand D., Dowler P., eds, Vol. 411, Astronomical Data Analysis Software and Systems XVIII. p. 251 (arXiv:0902.2850)
McAlpine S., et al., 2016, Astronomy and Computing, 15, 72
McGregor P. J., et al., 2003, in Iye M., Moorwood A. F. M., eds, Proc. SPIEVol. 4841, Instrument Design and Performance for Optical/Infrared Ground-based Telescopes. pp 1581–1591
Miller S. H., Bundy K., Sullivan M., Ellis R. S., Treu T., 2011, ApJ, 741, 115
Miller S. H., Ellis R. S., Sullivan M., Bundy K., Newman A. B., Treu T., 2012, ApJ, 753, 74
Mo H. J., Mao S., White S. D. M., 1998, MNRAS, 295, 319
Mobasher B., et al., 2015, ApJ, 808, 101
Molina J., Ibar E., Swinbank A. M., Sobral D., Best P. N., Smail I., Escala A., Cirasuolo M., 2017, MNRAS, 466, 892
Mortlock A., et al., 2013, MNRAS, 433, 1185
Munshi F., et al., 2013, ApJ, 766, 56
Muzzin A., et al., 2013, AJ Supplement Series, 206, 8
Navarro J. F., Frenk C. S., White S. D. M., 1997, ApJ, 490, 493
Obreschkow D., Glazebrook K., 2014, ApJ, 784, 26
Obreschkow D., et al., 2015, ApJ, 815, 97
Osterbrock D. E., Ferland G. J., 2006, Astrophysics of gaseous nebulae and active galactic nuclei
Paulino-Afonso A., Sobral D., Buitrago F., Afonso J., 2017, MNRAS, 465, 2717
Pelliccia D., Tresse L., Epinat B., Ilbert O., Scoville N., Amram P., Lemaux B. C., Zamorani G., 2017, A&A, 599, A25
Perna M., et al., 2018, A&A, 618, A36
Planck Collaboration et al., 2018, preprint, (arXiv:1807.06209)
Posti L., Pezzulli G., Fraternali F., Di Teodoro E. M., 2018, MNRAS, 475, 232
Qu Y., et al., 2017, MNRAS, 464, 1659
Reyes R., Mandelbaum R., Gunn J. E., Pizagno J., Lackner C. N., 2011, MNRAS, 417, 2347
Rizzo F., Fraternali F., Iorio G., 2018, MNRAS, 476, 2137
Romanowsky A. J., Fall S. M., 2012, ApJS, 203, 17
Roy N., et al., 2018, MNRAS, 480, 1057
Sandage A., 1986, in Star-forming Dwarf Galaxies and Related Objects. pp 31–40
Schaller M., et al., 2015, MNRAS, 451, 1247
Schaye J., et al., 2015a, MNRAS, 446, 521
Schaye J., et al., 2015b, MNRAS, 446, 521
Schreiber N. M. F., et al., 2018, AJl Supplement Series, 238, 21
Scoville N., et al., 2007, AJ Supplement Series, 172, 1
Sérsic J. L., 1963, Boletin de la Asociacion Argentina de Astronomia La Plata Argentina, 6, 41
Shibuya T., Ouchi M., Harikane Y., 2015, AJ Supplement Series, 219, 15
Simpson J. M., et al., 2017, VizieR Online Data Catalog, p. J/ApJ/788/125

Sobral D., Smail I., Best P. N., Geach J. E., Matsuda Y., Stott J. P., Cirasuolo M., Kurk J., 2013a, MNRAS, 428, 1128
Sobral D., et al., 2013b, ApJ, 779, 139
Sobral D., Best P. N., Smail I., Mobasher B., Stott J., Nisbet D., 2014, MNRAS, 437, 3516
Sobral D., et al., 2015, MNRAS, 451, 2303
Stark D. P., Swinbank A. M., Ellis R. S., Dye S., Smail I. R., Richard J., 2008, Nature, 455, 775
Steidel C. C., Adelberger K. L., Dickinson M., Giavalisco M., Pettini M., Kellogg M., 1998, ApJ, 492, 428
Stott J. P., Sobral D., Smail I., Bower R., Best P. N., Geach J. E., 2013, MNRAS, 430, 1158
Stott J. P., et al., 2016, MNRAS, 457, 1888
Sweet S. M., Fisher D. B., Glazebrook K., Obreschkow D., Lagos C. D. P., Wang L., 2018, preprint, (arXiv:1808.06269)
Swinbank A. M., Sobral D., Smail I., Geach J. E., Best P. N., McCarthy I. G., Crain R. A., Theuns T., 2012a, MNRAS, 426, 935
Swinbank A. M., Smail I., Sobral D., Theuns T., Best P. N., Geach J. E., 2012b, ApJ, 760
Swinbank A. M., et al., 2017, MNRAS,
Tiley A. L., et al., 2018, preprint, (arXiv:1810.07202)
Tinsley B. M., 1980, Fundamentals of Cosmic Physics, 5, 287
Toomre A., 1964, ApJ, 139, 1217
Toomre A., Toomre J., 1972, ApJ, 178, 623
Trayford J. W., Frenk C. S., Theuns T., Schaye J., Correa C., 2018, MNRAS, p. 2761
Tully R. B., Fisher J. R., 1977, A&A, 500, 105
Turner O. J., et al., 2017, MNRAS, 471, 1280
Übler H., et al., 2017, ApJ, 842, 121
Übler H., et al., 2018, ApJ, 854, L24
Van den Bosch F. C., Abel T., Croft R. A. C., Hernquist L., White S. D. M., 2002, ApJ, 576, 21
Wang L., et al., 2018, MNRAS, p. 2879
Weijmans A.-M., et al., 2014, MNRAS, 444, 3340
Weiner B. J., et al., 2006, ApJ, 653, 1027
Whitaker K. E., van Dokkum P. G., Brammer G., Franx M., 2012, ApJ, 754, L29
Williams R. J., Quadri R. F., Franx M., van Dokkum P., Labbé I., 2009, ApJ, 691, 1879
Wisnioski E., Förster Schreiber N. M., Wuyts S. e. a., 2015, apj, 799, 209
Wizinowich P. L., et al., 2006, in Society of Photo-Optical Instrumentation Engineers (SPIE) Conference Series. p. 627209
Wright S. A., Larkin J. E., 2007, in Afonso J., Ferguson H. C., Mobasher B., Norris R., eds, Astronomical Society of the Pacific Conference Series Vol. 380, Deepest Astronomical Surveys. p. 573
Wuyts S., et al., 2013, ApJ, 779, 135
Zhong G. H., Liang Y. C., Hammer F., Chen X. Y., Deng L. C., Flores H., 2010, A&A, 520, A69
da Cunha E., Charlot S., Elbaz D., 2008, MNRAS, 388, 1595
da Cunha E., et al., 2015, ApJ, 806, 110
van der Wel A., et al., 2014, ApJ, 788, 28

APPENDIX A: INTEGRATED GALAXY PROPERTIES

Table A1. (1) Target name, (2) Previously published name, 1 = Molina et al. (2017), 2 = Swinbank et al. (2012a), (3-4) Right Ascension and Declination in J2000 coordinates, (5) Spectroscopic redshift derived from the near infra-red integral field spectrum. Galaxies at $z \leq 2.5$ are detected in Hα, whilst those at $z \geq 3$ have their kinematics traced by the [OIII] emission line Sobral et al. (2013a, 2015); Khostovan et al. (2015), (6-8) Stellar properties derived using MagPhys da Cunha et al. (2008) using a Chabrier (2003) IMF, the Calzetti et al. (2000) reddening law and either constant or exponentially declining SFRs. Uncertainties on stellar properties derived from SEDs are dominated by systematic model assumptions.

Target	Published Name	R.A (J2000)	Decl. (J2000)	$z_{\rm spec}$	M_H (AB mag)	log(M$*$) ($M_\odot$)	$SFR_{\rm line}$ ($M_\odot yr^{-1}$)
SHIZELS–5	[1]SA22–54	22:22:23.04	+00:47:33.0	0.810	−22.74	10.1	6 ± 1
SHIZELS–6	[1]SA22–17	22:19:36.14	+00:34:07.9	0.812	−21.60	9.9	5 ± 2
SHIZELS–13	[1]SA22–28	22:15:36.31	+00:41:08.8	0.813	−22.28	9.9	7 ± 1
SHIZELS–15	[1]SA22-26	22:18:23.00	+01:00:22.1	0.815	−22.11	9.7	6 ± 2
SHIZELS–4	[2]SHIZELS–4	10:01:55.29	+02:14:03.3	0.830	−20.88	9.2	2 ± 1
SHIZELS–1	[2]SHIZELS–1	02:18:26.31	−04:47:01.6	0.843	−22.27	10.1	6 ± 1
SHIZELS–16	–	02:17:42.35	−05:15:05.1	1.339	–	10.4	17 ± 2
SHIZELS–17	[1]COS–16	10:00:49.01	+02:44:41.1	1.360	−22.19	9.5	9 ± 3
SHIZELS–10	[2]SHIZELS–10	02:17:39.02	−04:44:41.4	1.447	−22.62	10.1	9 ± 2
SHIZELS–7	[2]SHIZELS–7	02:17:00.34	−05:01:50.6	1.455	−23.32	10.6	12 ± 1
SHIZELS–8	[2]SHIZELS–8	02:18:20.96	−05:19:07.5	1.460	−23.66	10.3	16 ± 2
SHIZELS–9	[2]SHIZELS–9	02:17:12.99	−04:54:40.7	1.462	−24.01	10.8	26 ± 2
SHIZELS–12	[2]SHIZELS–12	02:19:01.45	−04:58:15.0	1.467	−23.90	10.7	21 ± 2
SHIZELS–18	–	02:17:34.20	−05:10:16.7	1.470	−22.34	10.3	49 ± 2
SHIZELS–19	[1]COS–30	09:59:11.57	+02:23:24.3	1.486	−24.01	10.3	13 ± 2
SHIZELS–11	[2]SHIZELS–11	02:18:21.23	−05:02:48.9	1.492	−25.69	10.9	23 ± 2
SHIZELS–20	–	09:59:37.96	+02:18:02.1	1.620	−22.35	10.8	33 ± 2
SHIZELS–2	–	02:19:25.50	−04:54:39.6	2.223	−22.14	9.8	18 ± 6
SHIZELS–3	–	10:00:27.69	+02:14:30.6	2.225	−21.25	9.0	21 ± 3
SHIZELS–21	[1]UDS–10	02:16:45.82	−05:02:45.0	2.237	−23.38	9.7	37 ± 4
SHIZELS–22	[1]SA22–01	22:19:16.06	+00:40:36.1	2.238	−23.57	10.2	34 ± 2
SHIZELS–23	[1]UDS–21	02:16:49.05	−05:03:20.8	2.239	−22.29	10.2	26 ± 5
SHIZELS–24	[1]UDS–17	02:16:55.32	−05:23:35.5	2.241	−24.46	9.8	60 ± 3
SHIZELS–14	[2]SHIZELS–14	10:00:51.58	+02:33:34.1	2.242	−25.35	9.5	81 ± 3
SHIZELS–25	[1]SA22–02	22:18:58.93	+00:05:58.3	2.253	−23.48	10.4	40 ± 2
SHIZELS–26	–	02:17:03.88	−05:16:19.5	3.227	−24.74	10.9	28 ± 17
SHIZELS–27	–	09:57:59.05	+02:38:19.7	3.238	−22.35	9.3	17 ± 10
SHIZELS–28	–	02:18:21.37	−05:19:16.7	3.252	−23.42	9.9	26 ± 15
SHIZELS–29	–	09:59:28.00	+02:44:34.0	3.253	−22.35	9.7	92 ± 55
SHIZELS–30	–	09:59:20.40	+02:25:21.1	3.256	−19.82	9.4	39 ± 23
SHIZELS–30	–	09:59:36.39	+02:17:44.0	3.263	−20.60	9.3	14 ± 8
SHIZELS–32	–	02:17:45.85	−05:25:45.4	3.273	−22.00	10.5	113 ± 2
SHIZELS–33	–	9:57:51.526	+02:36:37.9	3.278	−24.42	10.5	121 ± 2
SHIZELS–34	–	02:17:11.66	−04:54:44.7	3.300	−23.03	10.3	53 ± 32

APPENDIX B: INTEGRAL FIELD OBSERVATIONS.

Table B1. (1) Target Name as per Table A1, (2) Spectroscopic Hα or [OIII] redshift derived from spectrum, (3-5) Extra-galactic Field, Wavelength band and Integral Field Spectrograph used for spectroscopic observation, * = Laser Guide Star (LGS), otherwise Natural Guide Star (NGS), (6) Total on source integration time of integral field observations, (7) Integral field PSF size as measured from standard star observations in kpc, (8) Ancillary photometric data available for each target.

Target	z_{spec}	Extra-galactic Field	Band	IFU	t_{exp} (ks)	PSF R_h (kpc)	Broadband
SHIZELS–5	0.810	SA22	*J*	SINFONI	4.8	1.40	UKIDSS *K*
SHIZELS–6	0.812	SA22	*J*	SINFONI	4.8	1.40	UKIDSS *K*
SHIZELS–13	0.813	SA22	*J*	SINFONI	4.8	1.40	UKIDSS *K*
SHIZELS–15	0.815	SA22	*J*	SINFONI	4.8	1.40	UKIDSS *K*
SHIZELS–4	0.830	COSMOS	*J*	SINFONI	7.2	1.41	*HST* F160W, F814W
SHIZELS–1	0.843	UDS	*J*	SINFONI	7.2	1.42	UKIDSS *K*
SHIZELS–16	1.339	UDS	*H*	OSIRIS*	7.2	1.20	*HST* F125W, F160W, F814W
SHIZELS–17	1.360	COSMOS	*H*	SINFONI	7.2	1.20	*HST* F814W
SHIZELS–10	1.447	UDS	*H*	SINFONI	9.6	1.20	*HST* F140W, F606W
SHIZELS–7	1.455	UDS	*H*	SINFONI	9.6	1.20	*HST* F140W, F606W
SHIZELS–8	1.460	UDS	*H*	SINFONI	7.2	1.20	*HST* F140W, F606W
SHIZELS–9	1.462	UDS	*H*	SINFONI	9.6	1.20	*HST* F140W, F606W
SHIZELS–12	1.467	UDS	*H*	SINFONI	9.6	1.20	UKIDSS *K*
SHIZELS–18	1.470	UDS	*H*	OSIRIS*	7.2	1.20	*HST* F125W, F160W, F814W
SHIZELS–19	1.486	COSMOS	*H*	SINFONI	7.2	1.20	*HST* F160W, F814W
SHIZELS–11	1.492	UDS	*H*	SINFONI	7.2	1.20	*HST* F140W, F606W
SHIZELS–20	1.620	COSMOS	*H*	OSIRIS*	7.2	1.21	*HST* F814W
SHIZELS–2	2.223	UDS	*K*	SINFONI	14.4	0.74	*HST* F140W, F606W
SHIZELS–3	2.225	COSMOS	*K*	SINFONI	4.8	0.74	*HST* F140W, F606W
SHIZELS–21	2.237	UDS	*K*	2 NIFS & SINFONI	40.8	0.73	*HST* F140W, F606W
SHIZELS–22	2.238	SA22	*K*	SINFONI	9.6	0.73	UKIDSS *K*
SHIZELS–23	2.239	UDS	*K*	NIFS & SINFONI	27.6	0.73	UKIDSS *K*
SHIZELS–24	2.241	UDS	*K*	NIFS & SINFONI	27.6	0.73	UKIDSS *K*
SHIZELS–14	2.242	COSMOS	*K*	SINFONI	12.0	0.73	*HST* F140W, F606W, F814W
SHIZELS–25	2.253	SA22	*K*	SINFONI	9.6	0.73	UKIDSS *K*
SHIZELS–26	3.227	UDS	*K*	SINFONI	7.2	0.67	*HST* F125W, F160W, F814W
SHIZELS–27	3.238	COSMOS	*K*	SINFONI	19.8	0.67	*HST* F814W
SHIZELS–28	3.252	UDS	*K*	SINFONI	10.8	0.67	UKIDSS *K*
SHIZELS–29	3.253	COSMOS	*K*	SINFONI	9.6	0.67	*HST* F814W
SHIZELS–30	3.256	COSMOS	*K*	SINFONI	2.4	0.67	*HST* F814W
SHIZELS–30	3.263	COSMOS	*K*	SINFONI	13.2	0.67	*HST* F160W, F814W
SHIZELS–32	3.273	UDS	*K*	SINFONI	2.4	0.67	UKIDSS *K*
SHIZELS–33	3.278	UDS	*K*	SINFONI	2.4	0.67	*HST* F814W
SHIZELS–34	3.300	UDS	*K*	SINFONI	2.4	0.67	UKIDSS *K*

APPENDIX C: MORPHO-KINEMATIC PROPERTIES.

Table C1. (1) Target Name as per Table A1, (2-10) Morphological and Kinematic properties derived for our sample, (11) Qualify flag based on kinematic criteria (Section 3.10).

Target	R_h^{Sersic} (kpc)	Sérsic Index (n)	Axis Ratio	θ_{inc} (deg)	PA_{vel} (deg)	$Vrot_{2Rh}$ ($km\,s^{-1}$)	$\frac{Vcirc_{2Rh}}{Vrot_{2Rh}}$	σ_{median} ($km\,s^{-1}$)	$\frac{Vrot_{2Rh}}{\sigma_{median}}$	Quality Flag
SHIZELS–5	4.4 ± 1.5	0.9 ± 0.3	0.6 ± 0.1	52 ± 6	109 ± 44	101 ± 56	2.31	93 ± 9	1.1 ± 0.6	2
SHIZELS–6	4.3 ± 2.1	0.6 ± 0.2	0.9 ± 0.1	31 ± 12	91 ± 16	22 ± 22	4.85	44 ± 4	0.5 ± 0.5	3
SHIZELS–13	5.1 ± 1.2	0.9 ± 0.2	0.7 ± 0.1	47 ± 4	147 ± 30	29 ± 26	5.8	71 ± 7	0.4 ± 0.4	2
SHIZELS–15	3.3 ± 2.6	0.6 ± 0.4	0.8 ± 0.2	33 ± 16	145 ± 7	77 ± 20	1.64	47 ± 4	1.6 ± 0.5	2
SHIZELS–4	4.0 ± 2.9	0.9 ± 0.2	0.5 ± 0.1	62 ± 3	38 ± 46	21 ± 31	11.68	106 ± 10	0.2 ± 0.3	2
SHIZELS–1	2.8 ± 0.2	1.2 ± 0.1	0.7 ± 0.1	47 ± 1	21 ± 65	98 ± 37	2.28	86 ± 8	1.1 ± 0.5	1
SHIZELS–16	4.1 ± 0.8	1.6 ± 0.2	0.5 ± 0.1	60 ± 3	97 ± 34	63 ± 54	2.53	71 ± 7	0.9 ± 0.8	3
SHIZELS–17	1.7 ± 1.0	2.0 ± 0.4	0.4 ± 0.1	67 ± 4	103 ± 46	25 ± 23	7.94	87 ± 8	0.3 ± 0.3	3
SHIZELS–10	2.8 ± 0.6	2.0 ± 0.1	0.5 ± 0.2	61 ± 1	105 ± 23	30 ± 12	5.2	65 ± 6	0.5 ± 0.2	3
SHIZELS–7	4.9 ± 0.5	1.4 ± 0.1	0.7 ± 0.1	44 ± 1	154 ± 59	159 ± 69	1.4	70 ± 7	2.3 ± 1.0	1
SHIZELS–8	5.7 ± 0.4	0.6 ± 0.1	0.9 ± 0.1	28 ± 1	125 ± 20	143 ± 33	1.22	69 ± 6	2.1 ± 0.5	1
SHIZELS–9	5.9 ± 0.6	0.8 ± 0.1	0.7 ± 0.1	46 ± 2	71 ± 3	125 ± 45	1.57	67 ± 6	1.8 ± 0.7	2
SHIZELS–12	4.9 ± 0.2	0.6 ± 0.2	0.9 ± 0.1	31 ± 1	50 ± 31	379 ± 154	1.17	87 ± 8	4.4 ± 1.9	2
SHIZELS–18	4.4 ± 0.5	0.6 ± 0.2	0.7 ± 0.1	47 ± 2	122 ± 12	68 ± 25	4.05	111 ± 11	0.6 ± 0.2	2
SHIZELS–19	2.1 ± 0.5	0.9 ± 0.1	0.7 ± 0.2	45 ± 1	16 ± 6	96 ± 18	3.24	119 ± 11	0.8 ± 0.2	2
SHIZELS–11	5.5 ± 0.6	2.0 ± 0.1	0.9 ± 0.1	26 ± 3	58 ± 19	174 ± 134	1.44	88 ± 8	1.9 ± 1.6	1
SHIZELS–20	4.7 ± 3.1	1.0 ± 0.1	0.6 ± 0.1	58 ± 3	127 ± 18	159 ± 60	1.86	104 ± 10	1.5 ± 0.6	1
SHIZELS–2	1.2 ± 0.2	0.9 ± 0.1	0.8 ± 0.3	39 ± 1	148 ± 10	54 ± 7	2.99	62 ± 6	0.9 ± 0.2	2
SHIZELS–3	2.7 ± 0.7	2.0 ± 0.1	0.7 ± 0.3	49 ± 1	17 ± 71	38 ± 28	3.31	50 ± 5	0.7 ± 0.6	2
SHIZELS–21	5.8 ± 1.1	2.0 ± 0.3	0.5 ± 0.1	59 ± 4	39 ± 3	38 ± 25	5.78	97 ± 9	0.4 ± 0.3	2
SHIZELS–22	3.5 ± 3.4	0.8 ± 0.6	0.8 ± 0.2	34 ± 20	135 ± 48	16 ± 20	3.66	71 ± 7	0.2 ± 0.3	2
SHIZELS–23	3.6 ± 1.0	1.2 ± 0.2	0.6 ± 0.1	58 ± 2	24 ± 80	63 ± 13	2.87	69 ± 6	0.9 ± 0.2	2
SHIZELS–24	6.2 ± 2.0	2.0 ± 0.2	0.9 ± 0.1	28 ± 2	26 ± 64	82 ± 41	2.31	101 ± 10	0.8 ± 0.4	3
SHIZELS–14	4.5 ± 0.7	1.6 ± 0.1	0.5 ± 0.1	58 ± 3	74 ± 21	90 ± 40	3.06	143 ± 14	0.6 ± 0.3	3
SHIZELS–25	4.8 ± 3.0	0.6 ± 0.2	0.6 ± 0.2	54 ± 10	50 ± 35	86 ± 33	3.01	87 ± 8	1.0 ± 0.4	3
SHIZELS–26	2.2 ± 2.2	2.0 ± 0.2	0.6 ± 0.1	55 ± 2	164 ± 58	127 ± 24	4.43	221 ± 22	0.6 ± 0.1	3
SHIZELS–27	2.1 ± 1.4	0.6 ± 0.2	0.2 ± 0.1	90 ± 35	151 ± 43	52 ± 8	4.01	79 ± 7	0.7 ± 0.1	2
SHIZELS–28	3.0 ± 6.2	2.0 ± 0.4	0.8 ± 0.2	33 ± 13	142 ± 14	24 ± 36	4.52	68 ± 6	0.4 ± 0.5	3
SHIZELS–29	0.9 ± 0.5	1.5 ± 0.2	0.4 ± 0.3	72 ± 8	162 ± 29	37 ± 11	5.54	83 ± 8	0.4 ± 0.1	2
SHIZELS–30	1.8 ± 2.4	0.6 ± 0.1	0.6 ± 0.1	53 ± 2	151 ± 21	17 ± 14	12.91	111 ± 11	0.2 ± 0.1	3
SHIZELS–30	1.1 ± 0.5	2.0 ± 0.4	0.6 ± 0.1	58 ± 2	27 ± 51	24 ± 10	7.91	76 ± 7	0.3 ± 0.1	2
SHIZELS–32	2.8 ± 0.1	1.9 ± 0.2	0.9 ± 0.1	28 ± 3	36 ± 31	48 ± 42	2.83	40 ± 7	1.2 ± 1.2	2
SHIZELS–33	0.4 ± 2.1	2.0 ± 0.4	0.6 ± 0.3	55 ± 10	81 ± 12	64 ± 37	11.62	314 ± 31	0.2 ± 0.1	3
SHIZELS–34	2.5 ± 0.9	1.7 ± 0.4	0.7 ± 0.1	45 ± 4	36 ± 35	128 ± 54	2.33	108 ± 10	1.2 ± 0.5	1

APPENDIX D: KINEMATIC MAPS

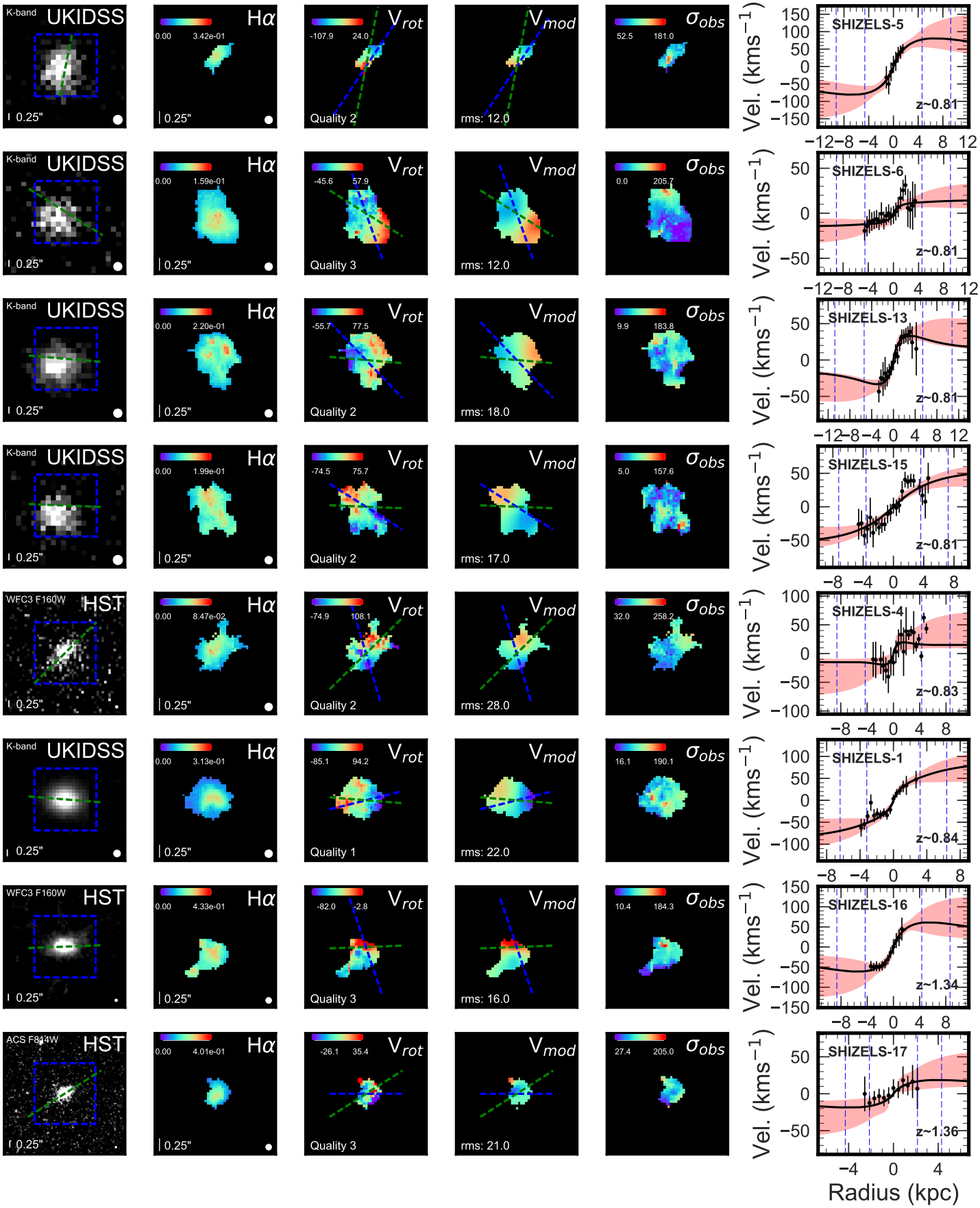

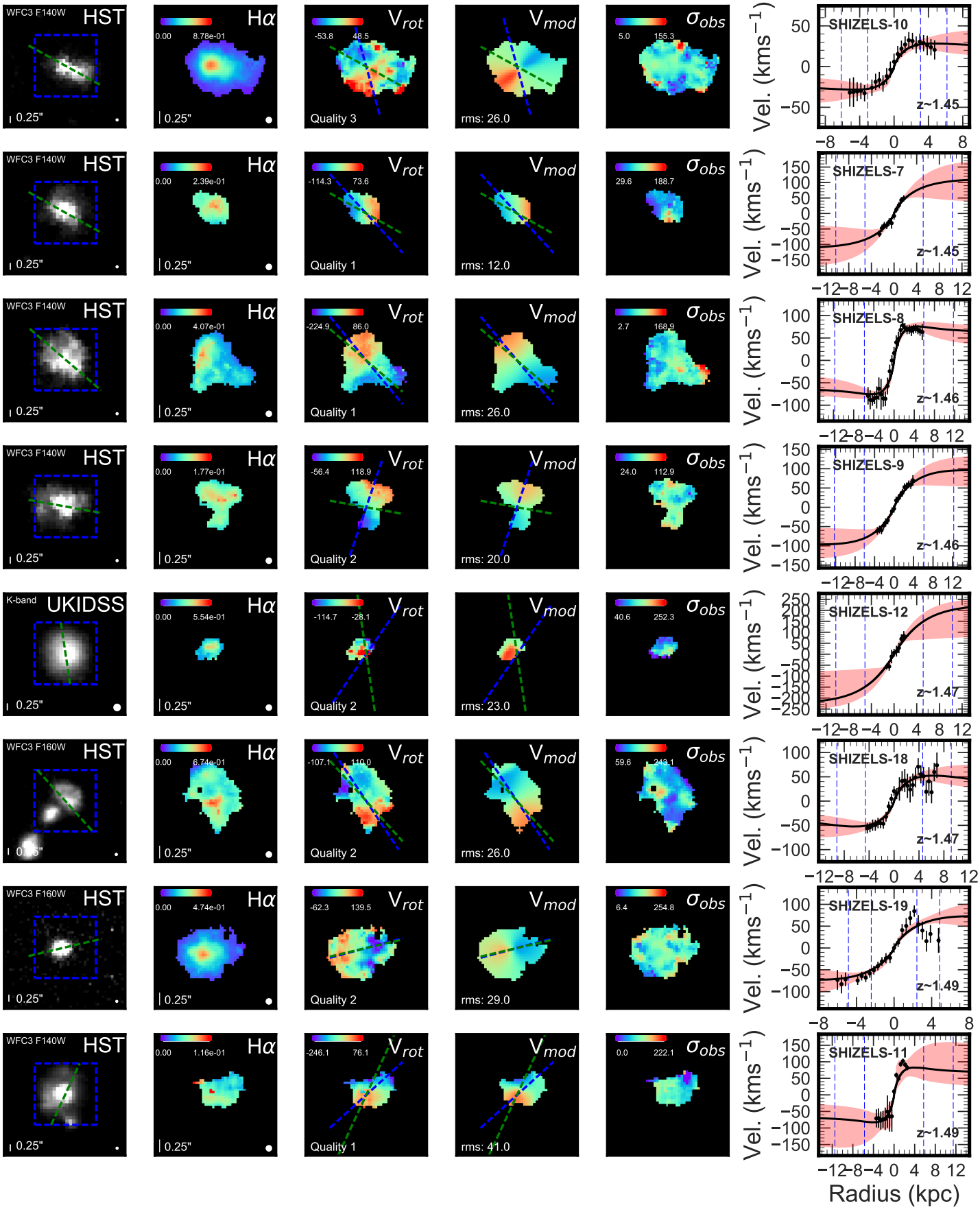
WFC3 F140W
HST
Hα
Vrot
Vmod
σobs
0.25"
Quality 3
rms: 26.0
SHIZELS-10
z~1.45
Quality 1
rms: 12.0
SHIZELS-7
z~1.45
Quality 1
rms: 26.0
SHIZELS-8
z~1.46
Quality 2
rms: 20.0
SHIZELS-9
z~1.46
K-band
UKIDSS
Quality 2
rms: 23.0
SHIZELS-12
z~1.47
WFC3 F160W
Quality 2
rms: 26.0
SHIZELS-18
z~1.47
Quality 2
rms: 29.0
SHIZELS-19
z~1.49
Quality 1
rms: 41.0
SHIZELS-11
z~1.49
Vel. (kms^{-1})
Radius (kpc)

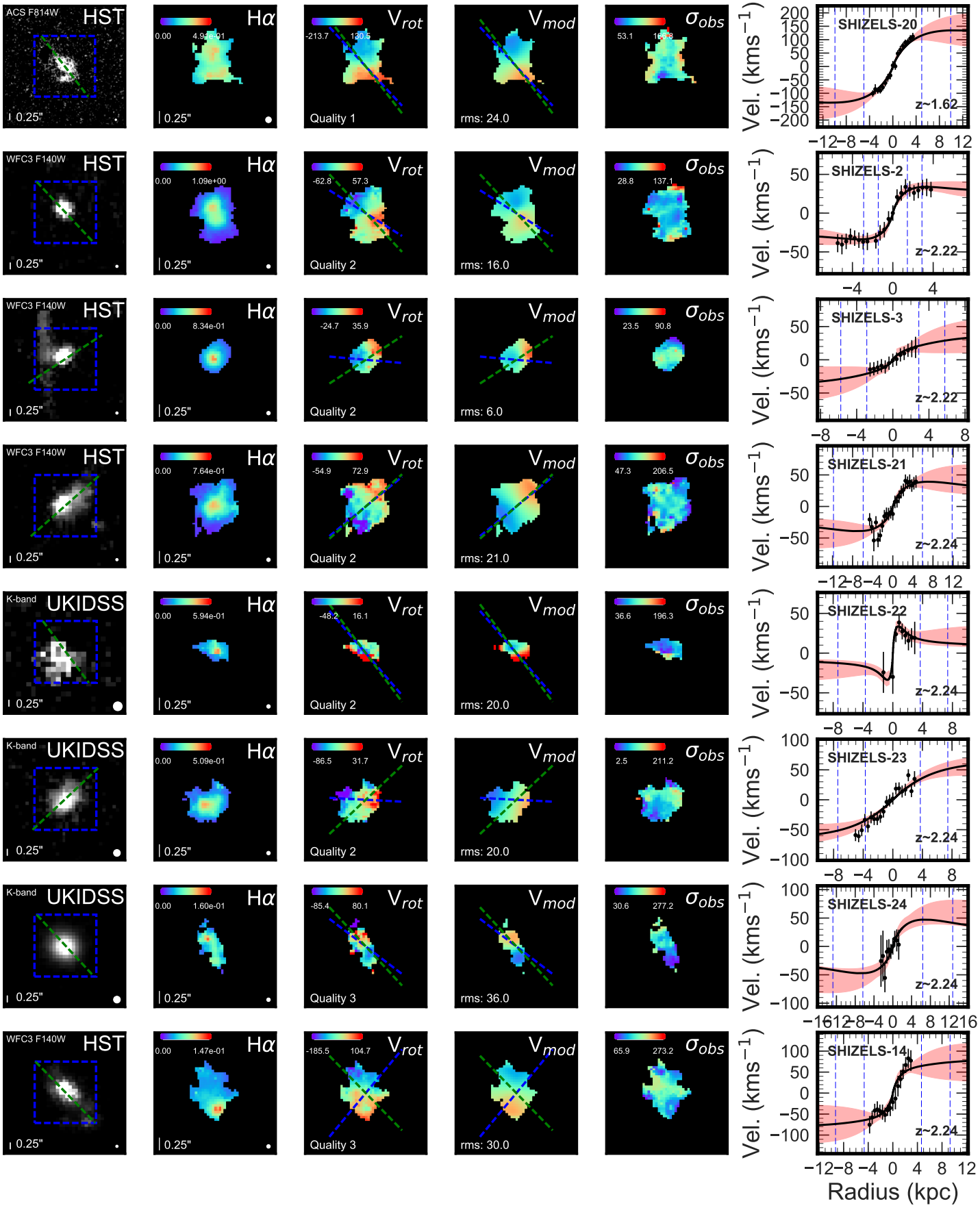
ACS F814W
HST
Hα
Vrot
Vmod
σobs
0.25"
Quality 1
rms: 24.0
SHIZELS-20
z~1.62
WFC3 F140W
Quality 2
rms: 16.0
SHIZELS-2
z~2.22
rms: 6.0
SHIZELS-3
z~2.22
rms: 21.0
SHIZELS-21
z~2.24
K-band
UKIDSS
rms: 20.0
SHIZELS-22
z~2.24
SHIZELS-23
z~2.24
Quality 3
rms: 36.0
SHIZELS-24
z~2.24
rms: 30.0
SHIZELS-14
z~2.24
Vel. (kms−1)
Radius (kpc)

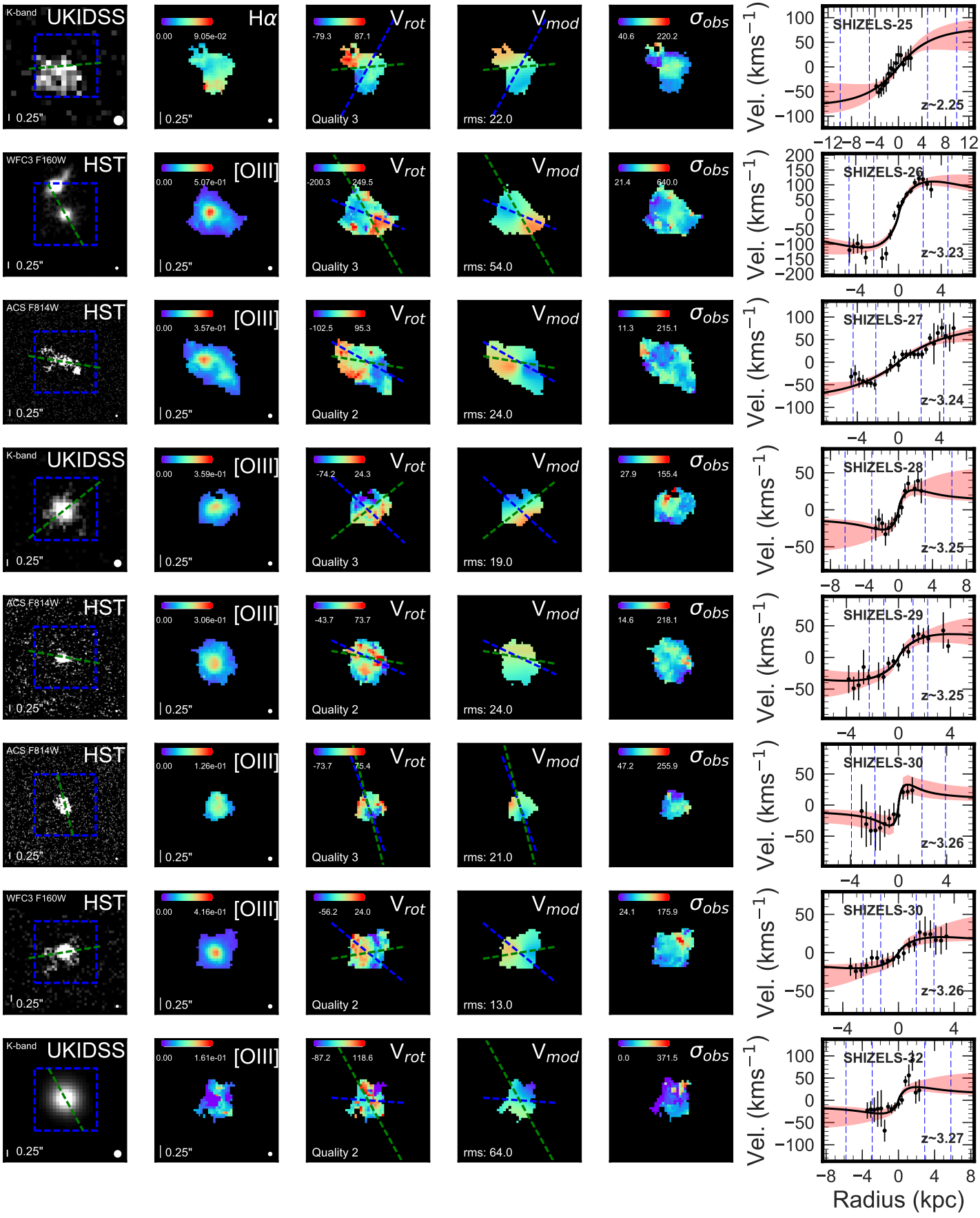
K-band UKIDSS
Hα
Vrot
Vmod
σobs
0.00 9.05e-02
-79.3 87.1
40.6 220.2
0.25"
Quality 3
rms: 22.0
SHIZELS-25
z~2.25
WFC3 F160W HST
[OIII]
0.00 5.07e-01
-200.3 249.5
21.4 640.0
Quality 3
rms: 54.0
SHIZELS-26
z~3.23
ACS F814W HST
0.00 3.57e-01
-102.5 95.3
11.3 215.1
Quality 2
rms: 24.0
SHIZELS-27
z~3.24
0.00 3.59e-01
-74.2 24.3
27.9 155.4
Quality 3
rms: 19.0
SHIZELS-28
z~3.25
0.00 3.06e-01
-43.7 73.7
14.6 218.1
Quality 2
rms: 24.0
SHIZELS-29
z~3.25
0.00 1.26e-01
-73.7 75.4
47.2 255.9
Quality 3
rms: 21.0
SHIZELS-30
z~3.26
0.00 4.16e-01
-56.2 24.0
24.1 175.9
Quality 2
rms: 13.0
SHIZELS-30
z~3.26
0.00 1.61e-01
-87.2 118.6
0.0 371.5
Quality 2
rms: 64.0
SHIZELS-32
z~3.27
Vel. (kms^{-1})
Radius (kpc)

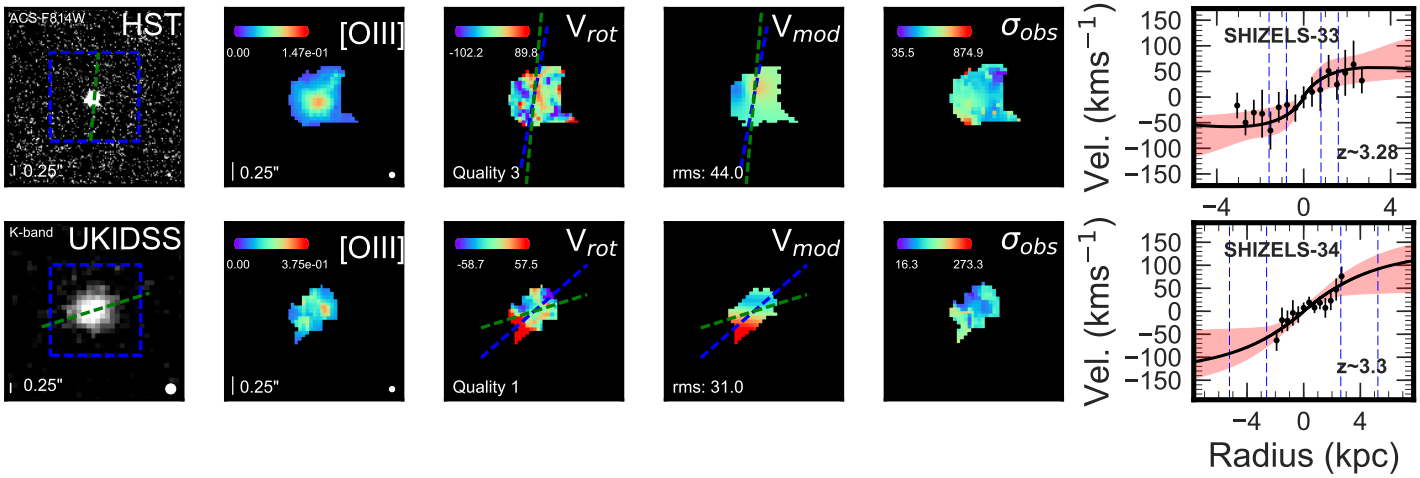

Figure D1: The spatially resolved galaxies in our sample order by redshift. From left to right; Broadband photometry of the galaxy (left), with PA_{im} (green dashed line) and data cube field of view (blue dashed square). Hα or [OIII] flux map, velocity map, velocity model and velocity dispersion map, derived from the emission line fitting. PA_{vel} (blue dashed line) and PA_{im} (green dashed line) axes plotted on the velocity map and model. Rotation curve extracted about kinematic position axis (right). Rotation curve shows lines of R_h and $2R_h$ derived from Sérsic fitting, as well 1σ error region (red) of rotation curve fit (black line).

APPENDIX E: BEAM-SMEARING CORRECTION

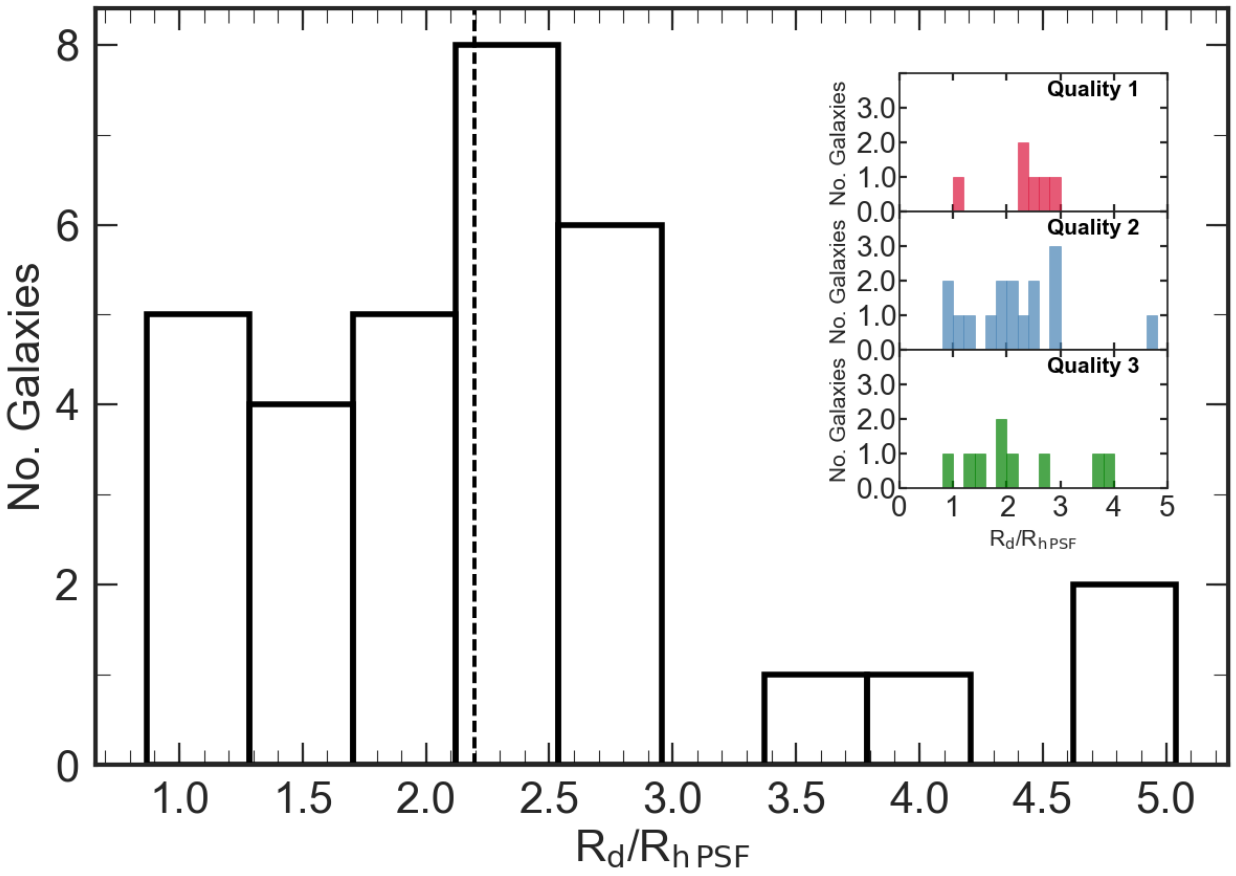

Figure E1: The ratio of $R_d/R_{h\,PSF}$ for each galaxy in the sample, as well as for the individual kinematic classes. The median ratio of the sample, black dashed line, is $< R_d/R_{h\,PSF} > = 2.17 \pm 0.18$. For the sample the median ratio of rotation velocity is $\frac{v_{out}}{v_0} = 0.99$, ranging from $\frac{v_{out}}{v_0} = 0.89 - 1.00$ whilst the median ratio of velocity dispersion is $\frac{v_{out}}{v_0} = 1.04$, ranging from $\frac{v_{out}}{v_0} = 1.00 - 1.11$.